This is a preprint, the final version is subject to change, of the American Mineralogist (MSA)
Cite as Authors (Year) Title. American Mineralogist, in press.
DOI: https://doi.org/10.2138/am-2020-7330

Revision 2

Thermodynamic and thermoelastic properties of wurtzite-ZnS by Density Functional Theory

Gianfranco Ulian, Daniele Moro and Giovanni Valdrè*

Dipartimento di Scienze Biologiche, Geologiche e Ambientali, Centro di Ricerche Interdisciplinari di Biomineralogia, Cristallografia e Biomateriali, Università di Bologna "Alma Mater Studiorum" Piazza di Porta San Donato 1, 40126 Bologna, Italy

* Corresponding author: giovanni.valdre@unibo.it

Abstract

In the present paper, we provide a detailed theoretical investigation on fundamental thermodynamic, thermomechanical and electronic properties of wurtzite ZnS between 0 – 20 GPa and 0 – 2000 K, obtained by *ab initio* Density Functional Theory and the B3LYP functional. Several properties, such as phonon dispersion relations, elastic and piezoelectric constants, thermodynamic and thermoelastic behaviors were calculated and reported. The analysis of the data via volume-integrated 3rd-order Birch-Murnaghan fitting resulted in K_0 = 72.17(4) GPa, K' = 3.87(1) and V_0 = 85.781(1) Å^3 at T = 0 K. The Born criteria for the mechanical stability of the mineral phase showed that wurtzite is unstable above about 19 GPa in static conditions. We calculated a direct band gap for wz-ZnS of 4.86 eV at zero compression, which became an indirect one by increasing pressure above 17 GPa. The results are in good agreement with the experimental and theoretical ones reported in literature, and further extend the knowledge of an important zinc sulphide phase, for both geological and industrial applications.

Keywords: Wurtzite ZnS, thermodynamic properties, elastic properties, electronic properties, Density Functional Theory, quasi-harmonic approximation.

This is a preprint, the final version is subject to change, of the American Mineralogist (MSA)
Cite as Authors (Year) Title. American Mineralogist, in press.
DOI: https://doi.org/10.2138/am-2020-7330

Introduction

Zinc sulphide ZnS belongs to the important family of the zinc monochalcogenides whose general formula is ZnX, with X = S, O, Se, Te or Cd. All the ZnX phases are isostructural and, from the mineralogical point of view, zinc sulphide is commonly found either as zinc-blende (zb-ZnS, mineralogical name sphalerite) or wurtzite (wz-ZnS). Both of them are closed-packed structure, but sphalerite belongs to the cubic system, with space group $F\bar{4}3m$ and cubic close packing (3C) with ABC sequence along <111> direction, whereas wz-ZnS has an hexagonal unit cell (2H) related to the space group $P6_3mc$ (Figure 1) with AB stacking along the [001] direction (Frey et al., 1986). In both zb- and wz-ZnS phases, each ion, either Zn^{2+} or S^{2-}, has a tetrahedral coordination. The structural difference between the two polymorphs is attributed to the stacking order of crystal planes along one of the C_3 axes and, according to Cardona et al. (2010), explains their very small difference of the enthalpies of formation. In addition, wurtzite is a high-temperature phase with respect to sphalerite, with a two-step 3C → 2H transition at temperature of about 1280 – 1300 K (Frey et al., 1986). There exists a third, high-pressure polymorph of ZnS, characterized by a halite-like structure (NaCl), with octahedral coordination of the ions, which is called rocksalt (rs) ZnS (space group $Fm\bar{3}m$).

In a very recent work we investigated in details by *ab initio* Density Functional Theory (DFT) simulations the thermodynamic and thermoelastic behavior of both cubic polymorphs of ZnS, finding that the zinc-blende to rock-salt phase transition occurs at 14.3 GPa at ~300 K (Ulian and Valdrè, 2019b), which was in very good agreement with the experimental result of Ono and Kikegawa (2018) in the same temperature condition (13.4 GPa).

The aim of the present paper is to extend the knowledge on the zinc sulphide polymorphs by providing thermodynamic, thermoelastic and electronic properties of the wurtzite ZnS phase. Indeed, there is a

continuous and still growing interest for its various and manifold applications. For example, zinc sulphide is an ore mineral, which is smelted to obtain zinc, and it is searched in the Earth crust by employing different approaches (Kowalczuk et al., 2018). One of them, which is increasingly used at global scale, is based on three-dimensional reflection seismic methods that provide high-resolution (order of metres to tens of metres) deep penetration data from about 300 m to 4 km (Malehmir et al., 2012; Bellefleur et al., 2015). A successful application of these methods requires detailed knowledge on the seismic wave propagation in the mineral structure, data that can be calculated from the elastic constant tensor.

In addition, wz-ZnS is the first discovered semiconductor and has very important and interesting electric/electrodynamic, mechanical and thermodynamic properties for applications in optoelectronic devices (*e.g.* displays, photodetectors) and in micro- and nanoelectromechanical systems (Özgür et al., 2005; Sang et al., 2013; Wang et al., 2017; Kandpal and Gupta, 2018; Ossai and Raghavan, 2018; Sinha et al., 2018; Xu et al., 2018). It is then not a surprise that wurtzite shares its name to all isostructural semiconductors of II-IV type. The remarkable chemical and physical features of this mineral phase, *e.g.* a wide band gap of about 3.87 eV (region of UV light), high optical transmittance of visible light, polar surfaces, piezoelectric behavious and good thermal stability, make wurtzite ZnS a highly valuable material (Cline et al., 1967; Adachi, 2005; Xu et al., 2018).

For all these reasons, it is crucial to carefully investigate the interplay of structural, elastic, thermodynamic and electronic properties in zinc sulphide at different pressure and temperature conditions, in particular for the wurtzite phase. This kind of research is often experimentally challenging, because many features of the phase, for the sake of an example the piezoelectric constants, can be measured only from single crystals of wurtzite. Such samples, when not available in nature, are usually difficult and expensive to grow in laboratory. In this context, a*b initio* theoretical simulations are a promising and well-established alternative, which can help the design of future experiments, *e.g.* aiding

experimentalists to screen and select the most promising materials for crystal growth purposes (Catti et al., 2003).

Following these considerations, in the present work we present a detailed and comprehensive analysis of the cited properties of wurtzite, conducted by *ab initio* Density Functional Theory simulations that follow and complete the one proposed in our previous work on sphalerite and rs-ZnS (Ulian and Valdrè, 2019b). The aim is providing a detailed set of data on several properties of wz-ZnS, obtained at the same level of theory to allow a direct and fruitful discussion on the polymorphs of zinc sulphide. Several aspects of wurtzite were investigated at the static (0 K) limit and we included the temperature effects by employing the so-called *quasi-harmonic approximation* on the lattice dynamics. More into details, we provide (i) the geometry of wurtzite both at equilibrium and after hydrostatic deformation, (ii) the equation of state (EoS) of the phase, (iii) the electronic band structure and density of states, the second-order elastic constants and the piezoelectric tensor, calculated as a function of applied pressure and (iv) the thermodynamic and thermoelastic behavior of wz-ZnS over the pressure and temperature range 0 – 20 GPa and 0 – 2000 K, respectively.

This paper is organized as follows. In the next section, the theory and algorithms used to calculate the above properties are briefly explained, providing the background of the work. Then, we present the obtained results, subdivided in small subsection for each property, and discuss them with previous experimental and theoretical researches on wurtzite. Indeed, the properties of this mineral were previously simulated with several theoretical approaches and we compared the effect of the computational parameters (basis set, Hamiltonians) on the calculated properties. Finally, we draw up the geological and technological implications of this work.

This is a preprint, the final version is subject to change, of the American Mineralogist (MSA)
Cite as Authors (Year) Title. American Mineralogist, in press.
DOI: https://doi.org/10.2138/am-2020-7330

Computational methods

In the present work, we performed *ab initio* Density Functional Theory (DFT) simulations with the CRYSTAL17 code (Dovesi et al., 2018). Since we were interested in the mechanical and thermodynamic properties of wz-ZnS, we chose the B3LYP hybrid functional (Lee et al., 1988; Becke, 1993a; Becke, 1993b) because of its well-known reliability with both structural and vibrational feature of solid systems (Ottonello et al., 2010; Prencipe et al., 2011; Belmonte et al., 2017). The description of the Zn and S orbitals is made via Gaussian-type functions, and we chose the Peitinger-Oliveira-Bredow (POB) double-ζ valence basis set with polarization (Peintinger et al., 2013; Ulian and Valdrè, 2019b). We employed a pruned grid consisting of 75 points and 974 angular points to evaluate the exchange–correlation contribution by numerical integration of the electron density and its gradient over the volume of the unit cell. We set the tolerances for truncation of the Coulomb and exchange integrals to 10^{-7} and 10^{-16}, which means that when the overlap between two atomic orbitals is lower than the threshold, the corresponding integral is either discarded or treated with less precision. We diagonalized the Hamiltonian matrix at 50 *k* points in the reciprocal space by employing a 8×8×8 Monkhorst-Pack net (Monkhorst and Pack, 1976).

Geometry optimization and equation of state

To calculate the equation of state of wurtzite at static conditions (0 K, no zero-point energy correction), we considered eleven unit cell volumes in the range $0.82V_0$ – $1.12V_0$, with V_0 being the equilibrium geometry. We calculated the starting (equilibrium) geometry by optimizing the unit cell parameters and the internal coordinates of the atoms at the same time, by employing a numerical gradient for the former and the analytical gradient method for the latter. The compressed and expanded unit cells for the equation of state were then optimized at constant volume by a symmetry preserving, variable cell-shape structure

relaxation approach (Ottonello et al., 2010). For both equilibrium and hydrostatically deformed unit cell, the geometry optimization was considered converged when the gradient and the maximum atomic displacement were lower than $1 \cdot 10^{-5}$ hartree bohr^{-1} and $4 \cdot 10^{-5}$ bohr, respectively, with respect to the previous optimization step.

The equation of state of the mineral was calculated by fitting the unit cell energy, E, as a function of the volume, V, using the volume-integrated 3rd-order Birch-Murnaghan (Hebbache and Zemzemi, 2004):

$$E = E_0 + \frac{9}{16} K_0 V_0 \left\{ K' \left(\eta^2 - 1 \right)^3 + \left[\left(\eta^2 - 1 \right)^2 \left(6 - 4\eta^2 \right) \right] \right\} \quad (1)$$

with $\eta = \left(V_0 / V \right)^{-1/3}$, K_0 is the bulk modulus of the system at both 0 GPa and 0 K, K' its pressure first derivative and V_0 the volume at zero pressure (to be not confused with the volume of the unit cell at equilibrium). E_0 is the energy of the unit cell at zero pressure and temperature.

The pressure corresponding to the compression/expansion of the unit cell was calculated by using these parameters in the well-known $P(V)$ formulation of the BM3 (Birch, 1947):

$$P = \frac{3}{2} K_0 \left[\eta^{-7/3} - \eta^{-5/3} \right] \left\{ 1 - \frac{3}{4} \left(4 - K' \right) \left(\eta^{-2/3} - 1 \right) \right\} + P_0 \quad (2)$$

Second-order elastic moduli

The elastic moduli for any crystal are obtained from the analytical derivatives of the total energy as a function of crystal deformation. To this aim, we employed a fully automated procedure, which was implemented in the CRYSTAL code (Perger et al., 2009; Perger, 2010). To remove the internal forces due to finite strain, the lattice parameters and the internal coordinates of the crystal are relaxed using analytic gradients (Doll, 2001; Doll et al., 2001). In this work, the elastic moduli were calculated using

7 points of displacement with a step of 0.005 Å. Since wurtzite has an hexagonal unit cell, the reference axis was oriented according to the guidelines of the Institute of Radio Engineering (IRE). More into details, during the simulations the Cartesian *x* and *z* axes of the reference system were oriented along the **a** and **c** lattice vectors of the unit cell, respectively (Brainerd, 1949).

We performed also the evaluation of the elastic moduli at different compressive states (*vide supra*). In this case, we employed a correction that considers the finite pre-stress, $\sigma_{pre} = P\delta_{ij}$, imposed to the system (Barron and Klein, 1965; Erba et al., 2014).

We calculated single-crystal directional behavior of the elastic properties of wurtzite following the approach suggested by Marmier and co-workers (2010).

Since most materials are not single crystals, we considered for practical applications definition of the polycrystalline elastic properties according to the formulations of both Nye (1957) and Voigt, Reuss and Hill, VRH (Hill, 1952). Pugh's ratio (k) and Vicker's hardness (H_V) were also calculated according to the formulation of Chen et al. (2011). The Pugh's ratio is a dimensionless empirical parameter, given by the ratio between the bulk (K) and the shear (μ) moduli, whose value represents an index of the ductile ($k > 1.75$) or brittle ($k < 1.75$) behavior of a material. H_V is related to the hardness of the mineral during indentation (resistance to plastic deformations).

The interested reader can find applications of the algorithms and formulations here briefly presented in other works (Ulian et al., 2014; Ulian and Valdrè, 2015c; Ulian and Valdrè, 2017; Ulian et al., 2018; Ulian and Valdrè, 2018c; Ulian and Valdrè, 2018b; Ulian and Valdrè, 2018a; Ulian and Valdrè, 2019a; Ulian and Valdrè, 2019b).

Finally, the direct piezoelectric e and dielectric ε tensors were evaluated through a coupled perturbed Kohn-Sham (CPKS) approach, as recently implemented in the CRYSTAL code (Baima et al., 2016).

This is a preprint, the final version is subject to change, of the American Mineralogist (MSA)
Cite as Authors (Year) Title. American Mineralogist, in press.
DOI: https://doi.org/10.2138/am-2020-7330

Lattice dynamics and thermodynamic properties

Harmonic phonon frequencies were calculated by diagonalization of the dynamical matrix using the direct space method, whose details are provided in specific literature (Parlinski et al., 1997; Wallace, 1998; Togo and Tanaka, 2015). We considered the effect of the longitudinal optical (LO) and transverse optical (TO) splitting in the phonon dispersion (Wang et al., 2010). The LO-TO splitting gives rise to a non-analytical contribution on the phonon bands and depends on the electronic (clamped nuclei) dielectric tensor ε_0 and on the Born effective charge tensor associated with each atom. We calculated both quantities through a coupled-perturbed Kohn-Sham (CPKS) approach (Pascale et al., 2004; Ferrero et al., 2008). Numerical convergence on the results was checked against three isotropic supercells with 32, 108 and 256 atoms (labelled as SC32, SC108 and SC256, respectively), leading to the sampling of 8, 27 and 64 **q** points in the reciprocal space, respectively. To increase the **q** point sampling and increase the quality of the thermodynamic results, we employed a Fourier interpolation method using an isotropic $4 \times 4 \times 4$ mesh (Dovesi et al., 2018), obtaining a total of 512, 1728 and 4096 **q** points for the SC32, SC108 and SC256 supercells, respectively.

Standard statistical thermodynamics on harmonic phonon frequencies can not provide a good description of thermodynamic and mechanic data at different *P-T* conditions. Thus, we employed the quasi-harmonic approximation (QHA), which describes the phonon of the system as volume-dependent, and overcomes the issue related to the harmonic approximation (*e.g.* zero thermal expansion). Several methods within the QHA framework have been proposed and employed in literature (Ottonello et al., 2010; Prencipe et al., 2011; Erba, 2014; Erba et al., 2015; Ulian and Valdrè, 2015a; Ulian and Valdrè, 2015b; Ulian and Valdrè, 2015c; Belmonte et al., 2017; Ulian and Valdre, 2018; Ulian and Valdrè, 2019b), and here we adopted the one discussed by Belmonte (2017) for periclase. The interested reader

can find complete details on this approach in QHA in the cited work whereas, for the sake of completeness, some of the main steps involved in the calculations are reported in the Appendix.

Results and Discussion

Equation of state

We reported in Table 1 the structural data on both the equilibrium geometry and the different unit cells of wurtzite under compression. The static energy versus unit cell volume curves, $E(V)$, are well fitted by the volume-integrated BM3 fit reported in Eq.(1), which resulted in K_0 = 72.17(4) GPa, K' = 3.87(1) and V_0 = 85.781(1) Å^3. The bulk modulus value is in good agreement with the very recent theoretical results of Valdez and co-workers (2019), who obtained K_0 = 74.3 GPa by employing plane-waves basis set and the Perdew-Burke-Ernzerhof (Perdew et al., 1996) DFT functional. In the work of Sharma et al. (2019), simulations with DFT/PBE plus Hubbard correction (DFT+U) resulted in bulk modulus and its pressure derivative 81.9 GPa and 3.96, respectively, which are also close to ours. It can be noted the systematic increase in the K_0 values previously obtained, which is a common figure when the PBE functional is adopted, related to the high repulsive core-valence exchange in Generalized-Gradient Approximation (GGA).

The zero-pressure unit cell parameters (a = 3.9233 Å, c = 6.3976 Å) are in good agreement with the theoretical ones calculated at the Hartree-Fock (HF) limit by Catti et al. (2003) (a = 3.982 Å, c = 6.500 Å) and the results of Valdez and co-workers (2019) obtained with DFT/PBE approach (a = 3.89 Å, c = 6.38 Å). It is worth noting that the pressure state of the equilibrium geometry is less than 10^{-5} GPa (10^{-1} atm), as observed from the forces acting on the unit cell after geometry optimization. The value reported in Table 1 was calculated from Eq.(2) using the BM3 parameters previously described.

Regarding the internal geometry of the mineral, there is an inverse relationship between pressure and the length of the non-equivalent Zn – S bonds (the minor labelled as d1 and the major as d2 in Table 1), whereas there is a direct proportionality with the S – Zn – S angle.

Electronic band structure

We reported the band gaps calculated at the B3LYP level at 0 K in Table 2. Band structure along the path Γ – A – L – M – Γ – A – H – K – A in the First Brillouin zone together with the total and orbital-projected density of states (DOSS) are presented graphically in Figure 2. At equilibrium (Figure 2a), the gap between the valence and conductive bands is of the direct type, with E_g = 4.87 eV and the increase of the hydrostatic pressure widens the band gap with a non-linear trend. At about 17 GPa and above (Figure 2b), the band gap becomes an indirect one, which is an electronic feature of the rock-salt (high-pressure) ZnS polymorph (Cardona et al., 2010; Ulian and Valdrè, 2019b). A similar result was obtained in previous simulations at the DFT/PW level of theory by Hu et al. (2008). The top of the valence band is dominated by the 3*p* states of sulphur, whereas the bottom of the conduction band is given mainly by 4*s* states of zinc.

Let us discuss these results with those in literature obtained with different approaches. The experimental value of the band gap of wurtzite is 3.87 eV (Madelung and Schulz, 1982). In this sense, the present result is overestimated by about 1 eV, which is not surprising due to the chosen Hamiltonian. The formulation of the hybrid functional B3LYP contains 20% of Hartree-Fock contribution to the total energy. Pure HF is known to highly overestimate the band gap of solids, but this effect is reduced by the GGA contribution that underestimates the same property. Indeed, recent calculations with pure GGA-PBE approach showed E_g values well below 2.5 eV (Karazhanov et al., 2006; Sharma et al., 2019; Valdez et al., 2019), and the addition of the Hubbard correction allowed obtaining results in better agreement

with experiments ($E_g \approx 3.87$ eV). Previous simulations with a semi-*ab initio* approach known as orthogonalised linear combination of atomic orbitals (OLCAO), based on the Kohn-Sham form of the exchange-correlation potential, resulted in a direct band gap of about 3.3 eV (Xu and Ching, 1993). Notwithstanding the different E_g values obtained with each approach, we obtained band structure features that are in good agreement with all previous simulations.

Elastic properties

As explained in the methods section, we calculated the second-order elastic moduli of wurtzite at each unit cell volume, including a correction for the pressure state of the system. For the sake of brevity, we reported in Table 3 only the results obtained at equilibrium. The complete results (elastic constants, piezoelectric constants, dielectric tensor and density), together with derived data (bulk, shear ad Young's moduli, Poisson's and Pugh ratio, Vickers hardness) are reported in Table S1 (Supporting Information).

It is possible to evaluate the mechanical stability of minerals from the values of the elastic moduli. For wurtzite, which has an hexagonal unit cell, the well-known Born stability criteria are given by the following three relations: (1) $\tilde{C}_{44} > 0$, (2) $\tilde{C}_{11} > \left|\tilde{C}_{12}\right|$ and (3) $2\tilde{C}_{13}^2 - \tilde{C}_{33}\left(\tilde{C}_{11} + \tilde{C}_{12}\right) < 0$, with $\tilde{C}_{\alpha\alpha} = C_{\alpha\alpha} - P$ for α = 1, 4 and $\tilde{C}_{1\alpha} = C_{1\alpha} + P$ (Born and Huang, 1954). As can be observed from Figure 3, the stability criteria (1) and (2) are not satisfied when the pressure is above 19.1 GPa and 20.5 GPa, respectively. In addition, the trend of curve $C_{44}(P)$ shows also an elastic softening with pressure. The third criterion, not shown in Figure 3, is respected in the investigated pressure range. This analysis shows that upon compression, the wurtzite phase is not stable above about 19 GPa at the static (0 K) limit, which is in agreement with previous simulations at the local-density approximation (LDA) level of theory (Ferahtia et al., 2014).

The elastic properties obtained with the DFT/B3LYP approach at equilibrium are in good agreement with previous theoretical results. With respect to Hartree-Fock (HF), we obtained higher values of the elastic moduli, whereas those calculated at generalized-gradient approximation level of theory (PBE functional) are generally lower, with the exception of the C_{12} modulus (Catti et al., 2003; Valdez et al., 2019). This is a common figure in DFT simulations, where standard GGA approaches results in smaller unit cell volume and higher bulk modulus (and consequently, elastic constants).

In comparison with experimental data, the present results are in excellent agreement, even if they were obtained at 0 K and without the inclusion of zero-point vibrational contributions (Cline et al., 1967; Uchida and Saito, 1972). The mean standard deviation on the calculated values is 2.9, which is lower respect the results of Catti et al. (2003), Ferahtia et al. (2014) and Valdez and co-workers (2019), calculated at the HF, LDA and generalized-gradient approximation with PBE functional, respectively.

Single-crystal mechanical properties calculated in different crystallographic directions are reported in Figure 4, together with previous theoretical and experimental results. For the sake of an example, in Figure 4a it is possible to observe that the maxima of the Young's modulus in wurtzite calculated on the $(10\bar{1}0)$ plane reside in the principal crystallographic directions, whereas the minima were calculated at 45° respect to **c**-axis direction. In addition, this phase shows an isotropic behavior in the (0001) plane (not shown in the figure).

As previously mentioned, we calculated and reported in Table S1 the bulk (K) and shear (μ), moduli for monocrystals, according to the formulation of Nye (1957). In Table 3 we reported only the results from the Voigt-Reuss-Hill (VRH) averages for polycrystalline aggregates (Hill, 1952), which includes Young's (E) modulus and Poisson's ratio.

The calculated Pugh's ratio and Vicker's hardness, k and H_V, respectively, are in good agreement with all previous experimental and theoretical results (Cline et al., 1967; Uchida and Saito, 1972; Catti et al.,

2003; Chen et al., 2011; Ferahtia et al., 2014; Valdez et al., 2019). It is interesting to note that the hardness and the *k* ratio of wurtzite decreases as pressure is raised, which means that the mineral becomes more ductile as pressure augments. In addition, the H_V value becomes negative at the maximum explored pressure, which is in agreement with the failure of the stability criteria previously discussed (see Table S1).

Regarding the piezoelectric constants, hexagonal crystals possess three independent tensor components, e_{33}, e_{31}, and e_{15}. The values calculated at the B3LYP level are in good agreement with both the experimental (Landolt-Börnstein, 1986) and previous theoretical data reported in literature (Catti et al., 2003; Ferahtia et al., 2014). The slightly larger discrepancy on the experimental e_{33} piezoelectric constant is due to the presence of defects in the real crystal sample of wurtzite used in the tests, as also pointed out by Catti and co-workers (2003).

Phonon properties

In the first step for the evaluation of the lattice dynamics of wurtzite, we calculated the Γ-point (**k** = 0) vibrational modes of the system, which were reported in Table 4. In details, the irreducible representation of the normal modes of wz-ZnS is the following:

$\Gamma_{tot} = 2A + 2B + 2E_1 + 2E_2$

with the first $A + E_1$ modes being acoustic. *A* and E_1 vibrational modes are active in both Raman and infrared spectroscopies and are subject to the LO-TO splitting. E_2 modes are Raman-active and *B* modes are silent.

It is interesting to note that the vibrational frequency of each mode increases with pressure, meaning positive isotropic mode-Grüneisen parameters $\gamma_i = -\left(\partial \ln \nu_i / \partial \ln V\right)$, with the subscript *i* indicating the

i-th vibrational mode. The only exception is the lowest E_2 normal mode, whose γ_i value is negative, showing that the frequency decreases by increasing pressure (decreasing unit cell volume). Considering the low frequency of this vibrational mode, this result suggests a possible phonon softening (negative frequency value) at higher pressure, which could be related to a phase transition from wurtzite to the rock-salt structure. Differently from elastic and thermodynamic analyses, it is not straightforward to establish the exact transition pressure from the *ab initio* trends of the $v(V)$ curves. However, they can represent a stability indicator, as we recently showed with the rock-salt phase of ZnS, which is phononically instable at low pressures (Ulian and Valdrè, 2019b).

The LO-TO splitting is quite remarkable for the modes interested by this phenomenon, with differences between the transverse optical – longitudinal optical frequencies (marked with Δ in Table 4) up to about 100 cm^{-1}.

Born charges evaluated at Γ-point for the equilibrium geometry of wurtzite are in agreement with the expected values for a zinc sulphide, namely we obtained +2.06 and –2.06 for zinc and sulphur, respectively, in good agreement with the ± 1.89 reported by Kang et al. (2017). The charges vary slightly by applying pressure to the system, with values of ±1.85 at 22.05 GPa and ±2.18 at -6.37 GPa.

As mentioned in the Methods section, to calculate reliable thermodynamic quantities we calculated the phonon dispersion relations using a direct space approach on supercells of increasing size. A graphical representation of the phonon bands and phonon density of states (DOS) is reported in Figure 5 at equilibrium geometry (Figure 5a) and at the maximum explored pressure (Figure 5b). In the M → Γ phonon branch it can be noted a very small inflection of an acoustic phonon, which is the result of some numerical noise related to the interpolation of the data during the construction of the phonon dispersion bands. The phonon DOS clearly shows that at low frequency the bands are dominated by zinc vibrations, whereas at higher wavenumbers sulphur plays the major role. The calculated phonon dispersion relations

and the phonon density of states are in good agreement with the previous experimental and theoretical results reported in literature (Hu et al., 2008; Bachmann et al., 2012).

In addition, we found a very good phonon continuity over the explored unit cell volumes (pressure), which means that the variations of the phonon frequency values as a function of volume are monotonic. Indeed, a 3rd-order polynomial fit on each phonon band resulted in a mean R^2 of $9.991 \cdot 10^{-1}$. This observation is important for the subsequent calculations of the mineral thermodynamics (*vide infra*).

Thermodynamic and thermoelastic properties

By combining the static equation of state and the phonon frequency dependence on volume (pressure), we are able to calculate several thermodynamic and thermoelastic data on wurtzite via the quasi-harmonic approximation (see Computational Methods section for details). We considered for this scope a pressure range of 0 – 20 GPa and temperatures between 0 K and 2000 K. It is worth noting that 0 K data obtained by means of the QHA approach are not the same as in static calculations, because here the zero-point thermal contribution is included in the treatment.

In Table 5, we present thermodynamic and elastic data of wurtzite calculated at 300 K as a function of pressure. Conversely, we report in Figure 6 some selected properties of interest, calculated at zero-pressure conditions, where it is possible to observe that the results are numerical converged when calculated on a supercell with 108 atoms. More into details, thermodynamic quantities are converged within 0.6%, whereas elastic properties (*e.g.* isothermal bulk modulus, K_T) within 1.2%. Albeit increasing the **k** sampling did not significantly increased the accuracy of the QHA approach, the following discussion and results will be focused on the results from SC256 (256 atoms in the supercell).

The calculated thermodynamics is in very good agreement with previous low- and high-temperature calorimetric measurements (Pankratz and King, 1965; Stuve, 1974; Robie and Hemingway, 1995). For example, the standard state entropy calculated by the present *ab initio* approach is 58.49 J mol^{-1} K^{-1}, which is very close to the measured value of 58.83 ± 0.17 J mol^{-1} K^{-1} (–0.6%). Also, the theoretical thermal evolution of both entropy (Figure 6a), heat capacity (Figure 6b) and enthalpy (as $H_T - H_{300}$, Figure 6c) fall between about 1 – 2% of the experimental values, a result consistent with previous theoretical prediction of these properties by *ab initio* methods (Belmonte et al., 2016).

Regarding the volumetric thermal expansion coefficient, it can be noted from Figure 6d that at very low temperatures the $\alpha_V(T)$ values are slightly negative, which is due not surprisingly to the E_2 phonon bands with negative Grüneisen parameter, as also reported by Biernacki and Scheffler (1989). At 300 K and 0 GPa, the calculated thermal expansion coefficient is 2.16×10^{-5}, which is in line with previous experimental and theoretical findings with α_V (300K) between 1.62×10^{-5} and 2.57×10^{-5} (Majumdar and Roy, 1965; Wang, 2006; Valdez et al., 2019).

We reported in Figure 6e the isothermal and adiabatic bulk moduli of wurtzite calculated at zero pressure as a function of temperature, which show the expected thermal trend. From the elastic properties point of view, these values represent the Reuss lower bound that can be calculated from the elastic moduli at different temperature and pressure states. At 300 K, we obtained K_T = 68.6(6) GPa, K_T' = 4.01(13) and K_S = 68.9 GPa, with isothermal bulk modulus that is slightly lower than those reported by Desgreniers et al. (2000) and by Chang and Barsch (1973), whose values were 80.1 GPa and 75.8 GPa, respectively.

We report in Figure 7, for the sake of completeness, some selected thermodynamic and thermoelastic properties of wurtzite as a function of both temperature and pressure, which could be useful for data extraction and comparison with future works.

Finally, we report in Figure 8 the zero-pressure relative volume variation with pressure at 300 K, in comparison with the experimental data of Desgreniers et al. (2000). It is possible to observe an excellent agreement between our DFT/B3LYP results and the experimental ones between 0 GPa and 5 GPa, then there is a small deviation (about 3% at 20 GPa), resulting in a softer behavior of wurtzite as a function of pressure. This discrepancy could be due to several reasons. The first one is that we simulated an ideal single-crystal of wurtzite, whereas the sample experimentally investigated was grinded to a fine powder prior the analysis in the diamond-anvil cell. Secondly, the authors reported a partial wurtzite → zinc-blende transformation during the grinding procedure, thus the powders contained a mixture of the two phases. Finally, when the wurtzite sample was compressed it transformed into the zinc-blende structure prior to a transition at higher pressure to the rock-salt structure and these two phases coexisted between from 12.4 to 13.5 GPa. These observations could also explain the discrepancy reported on the calculated bulk modulus.

Implications

Being wurtzite an important mineral phase in scientific and technological fields spanning from geology/mineralogy to material science, the present work provided deep insights on its thermodynamic, thermomechanic and electronic properties that can be useful for various applications. To cite some examples, the thermoelastic behavior of wz-ZnS showed that this mineral is unstable at high pressure and, considering also previous experimental and theoretical works, it should transforms to the rock-salt ZnS structure at several kilometers below the Earth's surface. The piezoelectric and elastic constants, electronic band structure and density of states are very important for industrial applications of wurtzite, because they could help designing a semiconductor material with tailored properties or, linked to the previous geological consideration, develop pressure sensors based on the direct-indirect band gap.

Wurtzite is also a model system for diamond-like structures presenting ionic bonds and many important minerals and semiconductors are isostructural with wz-ZnS, hence detailed elastic and thermodynamic data are useful to compare the effects of cationic/anionic substitutions and other crystal-chemical variations.

As a final note, the theoretical approach here employed, based on a combination of static (0 K) and thermal (QHA) methods, proved to be consistent and sound. The hybrid DFT functionals (as B3LYP) are also a very good choice for the prediction of thermodynamic properties of different kinds of minerals and compounds. This is important to obtain fundamental data at pressure and temperature conditions that are still difficult and expensive to be obtained experimentally. Indeed, a proper calibration of the static/QHA approach is a powerful predicting tool able to provide detailed analyses of phases of interest for different and manifold fields of applications.

Bibliographic references

Adachi, S. (2005) Properties of group IV, III-V, and II-VI semiconductors. John Wiley & Sons Ltd, Chirchester, England.

Bachmann, M., Czerner, M., Edalati-Boostan, S., and Heiliger, C. (2012) Ab initio calculations of phonon transport in ZnO and ZnS. European Physical Journal B, 85(5).

Baima, J., Erba, A., Maschio, L., Zicovich-Wilson, C.M., Dovesi, R., and Kirtman, B. (2016) Direct Piezoelectric Tensor of 3D Periodic Systems through a Coupled Perturbed Hartree-Fock/Kohn-Sham Method. Zeitschrift Fur Physikalische Chemie-International Journal of Research in Physical Chemistry & Chemical Physics, 230(5-7), 719-736.

Barron, T.H.K., and Klein, M.L. (1965) Second-order elastic constants of a solid under stress. Proceedings of the Physical Society, 85, 523-532.

Becke, A.D. (1993a) Density-Functional Thermochemistry .3. The Role of Exact Exchange. Journal of Chemical Physics, 98(7), 5648-5652.

-. (1993b) A New Mixing of Hartree-Fock and Local Density-Functional Theories. Journal of Chemical Physics, 98(2), 1372-1377.

Bellefleur, G., Schetselaar, E., White, D., Miah, K., and Dueck, P. (2015) 3D seismic imaging of the Lalor volcanogenic massive sulphide deposit, Manitoba, Canada. Geophysical Prospecting, 63(4), 813-832.

Belmonte, D., Gatti, C., Ottonello, G., Richet, P., and Zuccolini, M.V. (2016) Ab Initio Thermodynamic and Thermophysical Properties of Sodium Metasilicate, Na_2SiO_3, and Their Electron-Density and Electron-Pair-Density Counterparts. Journal of Physical Chemistry A, 120(44), 8881-8895.

Belmonte, D., Ottonello, G., Zuccolini, M.V., and Attene, M. (2017) The system MgO-Al_2O_3-SiO_2 under pressure: A computational study of melting relations and phase diagrams. Chemical Geology, 461, 54-64.

Biernacki, S., and Scheffler, M. (1989) Negative Thermal-Expansion of Diamond and Zincblende Semiconductors. Physical Review Letters, 63(3), 290-293.

Birch, F. (1947) Finite elastic strain of cubic crystal. Physical Review, 71, 809-824.

Born, M., and Huang, K. (1954) Dynamical Theory of Crystal Lattices. Clarendon Press, Oxford.

Brafman, O., and Mitra, S.S. (1968) Raman effect in wurtzite- and zinc-blende-type ZnS single crystals. Physical Review, 171, 931.

Brainerd, J.G. (1949) Standards on piezoelectric crystals. Proceedings of the I.R.E., 37, 1378-1395.

Cardona, M., Kremer, R.K., Lauck, R., Siegle, G., Munoz, A., Romero, A.H., and Schindler, A. (2010) Electronic, vibrational, and thermodynamic properties of ZnS with zinc-blende and rocksalt structure. Physical Review B, 81(7).

Catti, M., Noel, Y., and Dovesi, R. (2003) Full piezoelectric tensors of wurtzite and zinc blende ZnO and ZnS by first-principles calculations. Journal of Physics and Chemistry of Solids, 64(11), 2183-2190.

Chang, E., and Barsch, G.R. (1973) Pressure dependence of single crystal elastic constants and anharmonic properties of wurtzite. Journal of Physics and Chemistry of Solids, 34(9), 1543-1563.

Chen, X.Q., Niu, H., Li, D., and Li, Y. (2011) Modeling hardness of polycrystalline materials and bulk metallic glasses. Intermetallics, 19(9), 1275-1281.

Cline, C.F., Dunegan, H.L., and Henderson, G.W. (1967) Elastic constants of hexagonal BeO, ZnS, and CdSe. Journal of Applied Physics, 38, 1944-1948.

Desgreniers, S., Beaulieu, L., and Lepage, I. (2000) Pressure-induced structural changes in ZnS. Physical Review B, 61(13), 8726-8733.

Doll, K. (2001) Implementation of analytical Hartree-Fock gradients for periodic systems. Computer Physics Communications, 137, 74-78.

Doll, K., Harrison, N.M., and Saunders, V.R. (2001) Analytical Hartree-Fock gradients for periodic systems. Journal of Quantum Chemistry, 82(1), 1-13.

Dovesi, R., Erba, A., Orlando, R., Zicovich-Wilson, C.M., Civalleri, B., Maschio, L., Rerat, M., Casassa, S., Baima, J., Salustro, S., and Kirtman, B. (2018) Quantum-mechanical condensed matter simulations with CRYSTAL. Wiley Interdisciplinary Reviews-Computational Molecular Science, 8(4), E1360.

Erba, A. (2014) On combining temperature and pressure effects on structural properties of crystals with standard ab initio techniques. Journal of Chemical Physics, 141(12), 124115.

Erba, A., Mahmoud, A., Belmonte, D., and Dovesi, R. (2014) High pressure elastic properties of minerals from ab initio simulations: The case of pyrope, grossular and andradite silicate garnets. Journal of Chemical Physics, 140(12).

Erba, A., Maul, J., Demichelis, R., and Dovesi, R. (2015) Assessing thermochemical properties of materials through ab initio quantum-mechanical methods: the case of alpha-Al2O3. Physical Chemistry Chemical Physics, 17(17), 11670-11677.

Ferahtia, S., Saib, S., Bouarissa, N., and Benyettou, S. (2014) Structural parameters, elastic properties and piezoelectric constants of wurtzite ZnS and ZnSe under pressure. Superlattices and Microstructures, 67, 88-96.

Ferrero, M., Rerat, M., Orlando, R., and Dovesi, R. (2008) Coupled perturbed Hartree-Fock for periodic systems: The role of symmetry and related computational aspects. Journal of Chemical Physics, 128(1).

Frey, F., Jagodzinski, H., and Steger, G. (1986) On the Phase-Transformation Zinc Blends to Wurtzite. Bulletin De Mineralogie, 109(1-2), 117-129.

Hebbache, M., and Zemzemi, M. (2004) Ab initio study of high-pressure behavior of a low compressibility metal and a hard material: Osmium and diamond. Physical Review B, 70(22).

Hill, R. (1952) The elastic behaviour of a crystalline aggregate. Proceedings of the Physical Society, London, Section A, 65, 349-354.

Hu, C.E., Zeng, Z.Y., Cheng, Y., Chen, X.R., and Cai, L.C. (2008) First-principles calculations for electronic, optical and thermodynamic properties of ZnS. Chinese Physics B, 17(10), 3867-3874.

Kandpal, K., and Gupta, N. (2018) Perspective of zinc oxide based thin film transistors: A comprehensive review. Microelectronics International, 35(1), 52-63.

Kang, Y.S., Zhao, G.J., and Liang, X.X. (2017) First-principle study of the lattice dynamic and thermodynamic properties of Zn-based semiconductors with wurtzite structure. Physica B-Condensed Matter, 515, 51-55.

Karazhanov, S.Z., Ravindran, P., Kjekhus, A., Fjellvag, H., Grossner, U., and Svensson, B.G. (2006) Electronic structure and band parameters for ZnX (X = O, S, Se, Te). Journal of Crystal Growth, 287(1), 162-168.

Kowalczuk, P.B., Snook, B., Kleiv, R.A., and Aasly, K. (2018) Efficient extraction of copper and zinc from seafloor massive sulphide rock samples from the Loki's Castle area at the Arctic Mid-Ocean Ridge. Minerals Engineering, 115, 106-116.

Landolt-Börnstein. (1986) Landolt-Börnstein Tables. Springer, New York.

Lee, C.T., Yang, W.T., and Parr, R.G. (1988) Development of the Colle-Salvetti Correlation-Energy Formula into a Functional of the Electron-Density. Physical Review B, 37(2), 785-789.

Madelung, O., and Schulz, M. (1982) Numerical Data and Functional Relationships in Science and Technology. New Series. Group III: Crystal and Solid State Physics. Springer, Berlin.

Majumdar, A.J., and Roy, R. (1965) Thermal expansion of ZnS from 2 to 317 K. Journal of Applied Physics, 38, 1531-1534.

Malehmir, A., Durrheim, R., Bellefleur, G., Urosevic, M., Juhlin, C., White, D.J., Milkereit, B., and Campbell, G. (2012) Seismic methods in mineral exploration and mine planning: A general overview of past and present case histories and a look into the future. Geophysics, 77(5), Wc173-Wc190.

Marmier, A., Lethbridge, Z.A.D., Walton, R.I., Smith, C.W., Parker, S.C., and Evans, K.E. (2010) ElAM: A computer program for the analysis and representation of anisotropic elastic properties. Computer Physics Communications, 181(12), 2102-2115.

Monkhorst, H.J., and Pack, J.D. (1976) Special points for Brillouin-zone integrations. Physical Review B, 8, 5188-5192.

Nye, J.F. (1957) Physical properties of crystals. Oxford University Press, Oxford.

Ono, S., and Kikegawa, T. (2018) Phase transition of ZnS at high pressures and temperatures. Phase Transitions, 91(1), 9-14.

Ossai, C.I., and Raghavan, N. (2018) Nanostructure and nanomaterial characterization, growth mechanisms, and applications. Nanotechnology Reviews, 7(2), 209-231.

Ottonello, G., Civalleri, B., Ganguly, J., Perger, W.F., Belmonte, D., and Zuccolini, M.V. (2010) Thermo-chemical and thermo-physical properties of the high-pressure phase anhydrous B ($Mg_{14}Si_5O_{24}$): An ab-initio all-electron investigation. American Mineralogist, 95(4), 563-573.

Özgür, Ü., Alivov, Y.I., Liu, C., Teke, A., Reshchikov, M.A., Doğan, S., Avrutin, V., Cho, S.J., and Morkọ, H. (2005) A comprehensive review of ZnO materials and devices. Journal of Applied Physics, 98(4), 1-103.

Pankratz, L.B., and King, E.G. (1965) High-temperature heat contents and entropies of two zinc sulfides and four solid solutions of zinc and iron sulfides, 6708. U.S. Bureau of Mines.

Parlinski, K., Li, Z.Q., and Kawazoe, Y. (1997) First-principles determination of the soft mode in cubic ZrO2. Physical Review Letters, 78(21), 4063-4066.

Pascale, F., Zicovich-Wilson, C.M., Gejo, F.L., Civalleri, B., Orlando, R., and Dovesi, R. (2004) The calculation of the vibrational frequencies of crystalline compounds and its implementation in the CRYSTAL code. Journal of Computational Chemistry, 25(6), 888-897.

Peintinger, M.F., Oliveira, D.V., and Bredow, T. (2013) Consistent gaussian basis sets of Triple-Zeta valence with polarization quality for solid-State Calculations. Journal of Computational Chemistry, 34(6), 451-459.

Perdew, J.P., Burke, K., and Ernzerhof, M. (1996) Generalized gradient approximation made simple. Physical Review Letters, 77(18), 3865-3868.

Perger, W.F. (2010) First-Principles Calculation of Second-Order Elastic Constants and Equations of State for Lithium Azide, LiN_3, and Lead Azide, $Pb(N_3)_2$. International Journal of Quantum Chemistry, 110(10), 1916-1922.

Perger, W.F., Criswell, J., Civalleri, B., and Dovesi, R. (2009) Ab-initio calculation of elastic constants of crystalline systems with the CRYSTAL code. Computer Physics Communications, 180(10), 1753-1759.

Prencipe, M., Scanavino, I., Nestola, F., Merlini, M., Civalleri, B., Bruno, M., and Dovesi, R. (2011) High-pressure thermo-elastic properties of beryl (Al4Be6Si12O36) from ab initio calculations, and observations about the source of thermal expansion. Physics and Chemistry of Minerals, 38(3), 223-239.

Robie, R.A., and Hemingway, B.S. (1995) Thermodynamic Properties of Minerals and Related Substances at 298.15 K and 1 Bar (10^5 Pascals) Pressures and at Higher Temperatures, U.S. Geological Survey Bulletin 2131. U.S. Geological Survey, Denver, Colorado, VA, USA.

Sang, L., Liao, M., and Sumiya, M. (2013) A comprehensive review of semiconductor ultraviolet photodetectors: From thin film to one-dimensional nanostructures. Sensors (Switzerland), 13(8), 10482-10518.

Sharma, M., Mishra, D., and Kumar, J. (2019) First-principles study of the structural and electronic properties of bulk ZnS and small ZnnSn nanoclusters in the framework of the DFT plus U method. Physical Review B, 100(4), 12.

Sinha, T., Lilhare, D., and Khare, A. (2018) Effects of Various Parameters on Structural and Optical Properties of CBD-Grown ZnS Thin Films: A Review. Journal of Electronic Materials, 47(2), 1730-1751.

Stuve, J.M. (1974) Low-temperature heat capacities of sphalerite and wurtzite, 7940. U. S. Bureau of Mines.

Togo, A., and Tanaka, I. (2015) First principles phonon calculations in materials science. Scripta Materialia, 108, 1-5.

Uchida, N., and Saito, S. (1972) Elastic and photoelastic constants of α-ZnS. Journal of Applied Physics, 43(3), 971-976.

Ulian, G., Moro, D., and Valdrè, G. (2018) First principle investigation of the mechanical properties of natural layered nanocomposite: Clinochlore as a model system for heterodesmic structures. Composite Structures, 202, 551-558.

Ulian, G., Tosoni, S., and Valdrè, G. (2014) The compressional behaviour and the mechanical properties of talc [$Mg_3Si_4O_{10}(OH)_2$]: a density functional theory investigation. Physics and Chemistry of Minerals, 41(8), 639-650.

Ulian, G., and Valdre, G. (2018) Equation of state of hexagonal hydroxylapatite (P6(3)) as obtained from density functional theory simulations. International Journal of Quantum Chemistry, 118(12), e25553.

Ulian, G., and Valdrè, G. (2015a) Density functional investigation of the thermo-physical and thermo-chemical properties of 2M(1) muscovite. American Mineralogist, 100(4), 935-944.

-. (2015b) Density functional investigation of the thermophysical and thermochemical properties of talc Mg3Si4O10(OH)(2). Physics and Chemistry of Minerals, 42(2), 151-162.

-. (2015c) Structural, vibrational and thermophysical properties of pyrophyllite by semi-empirical density functional modelling. Physics and Chemistry of Minerals, 42(7), 609-627.

Ulian, G., and Valdrè, G. (2017) Effects of fluorine content on the elastic behavior of topaz Al2SiO4(F,OH)(2). American Mineralogist, 102(1-2), 347-356.

-. (2018a) Anisotropy and directional elastic behavior data obtained from the second-order elastic constants of portlandite Ca(OH)2 and brucite Mg(OH)2. Data in Brief, 21, 1375-1380.

-. (2018b) Effect of mechanical stress on the Raman and Infrared bands of hydroxylapatite: a quantum mechanical first principle investigation. Journal of the Mechanical Behavior of Biomedical Materials, 77, 683-692.

-. (2018c) Second-order elastic constants of hexagonal hydroxylapatite ($P6_3$) from ab initio quantum mechanics: comparison between DFT functionals and basis sets. International Journal of Quantum Chemistry, 118(5), e25500.

-. (2019a) Equation of state and second-order elastic constants of portlandite $Ca(OH)_2$ and brucite $Mg(OH)_2$. Physics and Chemistry of Minerals, 46(2), 101-117.

-. (2019b) Thermomechanical, electronic and thermodynamic properties of ZnS cubic polymorphs: an ab initio investigation on the zinc-blende – rock-salt phase transition. Acta Crystallographica Section B, 75, 1042 - 1059.

Valdez, L.A., Caravaca, M.A., and Casali, R.A. (2019) Ab-initio study of elastic anisotropy, hardness and volumetric thermal expansion coefficient of ZnO, ZnS, ZnSe in wurtzite and zinc blende phases. Journal of Physics and Chemistry of Solids, 134, 245-254.

Wallace, D.W. (1998) Thermodynamics of Crystals. Dover Publications.

Wang, K., Xub, X., Ma, L., Wang, A., Wang, R., Luo, J., and Wen, S. (2017) Studies on triboluminescence emission characteristics of various kinds of bulk ZnS crystals. Journal of Luminescence, 186, 307-311.

Wang, S.Q. (2006) First-principles study of the anisotropic thermal expansion of wurtzite ZnS. Applied Physics Letters, 88(6).

Wang, Y., Wang, J.J., Wang, W.Y., Mei, Z.G., Shang, S.L., Chen, L.Q., and Liu, Z.K. (2010) A mixed-space approach to first-principles calculations of phonon frequencies for polar materials. Journal of Physics-Condensed Matter, 22(20).

Xu, X., Li, S., Chen, J., Cai, S., Long, Z., and Fang, X. (2018) Design Principles and Material Engineering of ZnS for Optoelectronic Devices and Catalysis. Advanced Functional Materials, 28(36).

Xu, Y.N., and Ching, W.Y. (1993) Electronic, optical, and structural properties of some wurtzite crystals. Physical Review B, 48(7), 4335-4351.

This is a preprint, the final version is subject to change, of the American Mineralogist (MSA)
Cite as Authors (Year) Title. American Mineralogist, in press.
DOI: https://doi.org/10.2138/am-2020-7330

Figure captions

Figure 1. Wurtzite unit cell model, with zinc and sulphur atoms colored in grey and yellow, respectively.

Figure 2. Electronic band structure and density of states of wurtzite (a) at equilibrium and (b) at P = 22 GPa, both at 0 K.

Figure 3. Graphical representation of the mechanical stability criteria $\tilde{C}_{44} > 0$ and $\tilde{C}_{11} > \left|\tilde{C}_{12}\right|$ of wurtzite under pressure.

Figure 4. (a) Young's modulus (GPa), (b) linear compressibility ($1/K$, GPa^{-1}), (c) shear modulus (GPa) and (d) Poisson's ratio for the $(10\bar{1}0)$ plane of wurtzite. DFT/PBE (Valdez et al., 2019) and Hartree-Fock (Catti et al., 2003), together with the experimental results of Cline and co-workers (1967) (red line) and of Uchida and Saito (1972) (purple line) are reported for a graphical comparison. In (c) and (d), the continuous lines are related to the maximum values, whereas the dashed ones to the minimum values.

Figure 5. Phonon dispersion and phonon density of states (DOS) of wurtzite ZnS calculated (a) at equilibrium geometry and (b) at 22.05 GPa.

Figure 6. Selected thermodynamic and elastic properties of wurtzite at 0 GPa between 0 K and 2000 K, calculated on supercells (SC) of increasing size (32, 108 and 256 atoms in SC32, SC108 and SC265, respectively). (a) Entropy, (b) isochoric, C_V, and isobaric, C_P, heat capacities, (c) enthalpy (as $H_T - H_{300}$), (d) volumetric thermal expansion coefficient, α_V and (e) isothermal, K_T, and adiabatic, K_S, bulk moduli (corresponding to the Reuss lower bound).

Figure 7. Contour maps in the pressure and temperature ranges 0 – 20 GPa and 0 – 2000 K, respectively, of (a) adiabatic bulk modulus (Reuss lower bound), (b) entropy, (c) enthalpy and (d) Gibbs free energy. In (c) and (d), the reported difference is related to the wurtzite at zero pressure and temperature.

Figure 8. (a) Relative unit cell of wurtzite at 300 K as a function of pressure, calculated at the DFT/B3LYP level of theory, compared to the experimental results of Desgreniers et al. (2000). (b) Contour maps of the wurtzite unit cell in the pressure and temperature ranges 0 – 20 GPa and 0 – 2000 K, respectively.

Appendix

Let us briefly recall the quasi-harmonic approximation approach used to obtain *P*-*T*-*V* thermodynamic and thermoelastic properties of mineral phases. The main quantity involved in these calculations is the Helmholtz free energy (*F*) of the system, which is given by:

$$F(V,T) = U_0(V) + F^{QHA}(V,T) \tag{3}$$

where $U_0(V)$ is the static energy of the crystal at $T = 0$ K. F^{QHA} is calculated as:

$$F^{QHA}(V,T) = U_0^{ZP}(V) + \beta^{-1}\sum_{\mathbf{q}p}\left[\ln\left(1-e^{\beta\hbar\omega_{\mathbf{q}p}(V)}\right)\right] \tag{4}$$

with $U_0^{ZP}(V) = \sum_{\mathbf{q}p}\hbar\omega_{\mathbf{q}p}(V)/2$ and $\beta = 1/k_BT$, **q** indicates the sampled *k*-points in reciprocal space and ω_p is the *p*-th harmonic frequency.

By definition, the pressure state of the system is the first derivative of Eq.(3):

$$P(V,T) = -\frac{\partial U_0(V)}{\partial V} - \frac{\partial F^{QHA}(V,T)}{\partial V} \tag{5}$$

Eq.(4) and Eq.(5) gives us the possibility to obtain the volume of the system at any desired pressure and temperature condition by minimizing the Helmholtz free energy of the crystal. This task can be accomplished by using different approaches, such as numerical first derivative of Eq.(5) (Erba, 2014). Here we employed the phenomenological approach of Belmonte (2017), using the volume-integrated 3rd-

order Birch-Murnaghan EoS formulation reported in Eq.(1) to fit the $F(V, T)$ curves from Eq.(3). Besides providing a description of the evolution of the crystal in pressure and temperature closer to the experimental approaches, this method has the advantages of being both more robust and able to provide at the same time the mechanical properties of the system (K_T and K').

Then, other properties, such as the volumetric thermal expansion, the isothermal bulk modulus, the isobaric heat capacity and the adiabatic bulk modulus can be straightforwardly calculated as. respectively:

$$\alpha_V(T) = -\frac{1}{V(T)}\left(\frac{\partial V(T)}{\partial T}\right)_P \tag{6}$$

$$C_P(T) = C_V(T) + \alpha_V^2(T) K_T(T) V(T) T \tag{7}$$

$$K_S(T) = K_T(T) + \frac{\alpha_V^2(T) V(T) K_T^2(T) T}{C_V(T)}. \tag{8}$$

In the present work, the properties related to Eqs.(7) and (8) were calculated using the molar volume (Å^3 mol^{-1}) and isochoric heat capacity (J mol^{-1} K^{-1}).

List of tables

Table 1. Wurtzite unit cell volume, lattice parameters and bond distances and angles calculated at different hydrostatic compressions and in static conditions.

P (Gpa)	V (Å^3)	a (Å)	c (Å)	d1 (Å)	d2 (Å)	θ (°)
22.1	70.145	3.6620	6.0397	2.251	2.248	110.05
17.2	72.495	3.7072	6.0908	2.275	2.275	109.80
12.5	75.142	3.7550	6.1538	2.302	2.303	109.64
8.5	77.856	3.8020	6.2192	2.329	2.332	109.52
5.1	80.635	3.8485	6.2864	2.356	2.360	109.43
1.8	83.792	3.8997	6.3621	2.386	2.391	109.34
0.4	*85.282*	*3.9233*	*6.3976*	2.400	2.405	109.31
-0.5	86.400	3.9408	6.4240	2.411	2.416	109.29
-2.8	89.387	3.9867	6.4940	2.438	2.444	109.24
-4.7	92.441	4.0324	6.5645	2.465	2.472	109.20
-6.4	95.563	4.0780	6.6354	2.492	2.500	109.15

Notes: d1 and d2 are referred to Zn – S bonds, whereas θ is the S – Zn – S bond angle. Pressure values were obtained using the volume-integrated EoS parameters in the pressure-volume formulation of the 3rd-order Birch-Murnaghan equation.

Table 2. Calculated band gap (E_g, eV) and band gap type of wurtzite at different compression states.

P (GPa)	E_g (eV)	Type
22.1	5.652	indirect
17.2	5.641	indirect
12.5	5.508	direct
8.5	5.372	direct
5.1	5.174	direct
1.8	4.957	direct
0.4	4.862	direct
-0.5	4.788	direct
-2.8	4.600	direct
-4.7	4.415	direct
-6.4	4.235	direct

Table 3. Second-order elastic constants (reported in GPa), piezoelectric constants (C m^{-2}) and polycrystalline averages of wurtzite at equilibrium geometry. K, μ, E υ and are the polycrystalline averages of the bulk modulus (GPa), shear modulus (GPa), Young's modulus (GPa) and Poisson's ratio, respectively. k is the Pugh ratio μ/K and H_v is the Vickers hardness (GPa).

	B3LYP[a]	PBE[b]	LDA[c]	HF[d]	Exp[e]	Exp[f]	Exp[g]
C_{11}	119.1	125.7	135.46	118	124	122	
C_{12}	55.8	52.86	65.89	52	60	59	
C_{13}	44.4	47.5	51.63	39	45	46	
C_{33}	136.7	135.2	160.77	135	140	138	
C_{44}	28.1	33.6	29.73	31	29	28	
e_{33}	0.25		0.161	0.18			0.34
e_{31}	-0.16		-0.160	-0.13			-0.10
e_{15}	-0.12		-0.105	-0.13			-0.08
K	73.5	75.8	85.52	70.1	76.4	76.0	
μ	32.6	36.5	35.57	34.6	33.3	32.4	
E	85.3	94.3	93.71	89.2	87.3	85.1	
υ	0.31	0.29	0.32	0.29	0.31	0.31	
k	0.44	0.49	0.42	0.48	0.44	0.43	
H_v	2.9	4.0	2.8	4.0	2.9	2.6	

Notes: [a] Present work; [b] Valdez et al. (2019); [c] Ferahtia et al. (2014); [d] Catti et al. (2003); [e] Cline et al. (1967); [f] Uchida and Saito (1972); [g] Landolt-Börnstein (1986)

Table 4. Γ-point frequencies (cm^{-1}) of wurtzite-2H at different pressures, calculated at the DFT/B3LYP level of theory taking into account the LO-TO splitting.

Modes		**Pressure (GPa)**											**DFT**†	**Exp**‡
		22.1	*17.2*	*12.5*	*8.5*	*5.1*	*1.8*	*0.4*	*-0.5*	*-2.8*	*-4.7*	*-6.4*		
E_2	(*TO*)	47.7	57.1	64.2	69.8	73.9	77.5	78.9	79.7	81.5	82.5	83.3	72.9	72.5
B	(*TO*)	239.3	232.6	226.4	220.5	214.7	207.6	204.6	202.3	196.2	190.0	183.6	193.8	-
A	(*TO*)	366.6	346.7	327.3	308.6	291.2	272.8	264.5	258.3	242.7	227.8	213.2	277.6	273.3
	(*LO*)	435.2	419.1	403.5	388.9	375.4	361.1	354.8	350.1	338.3	327.2	316.5	332.9	351.1
	Δ	68.6	72.4	76.3	80.3	84.2	88.4	90.3	91.8	95.6	99.4	103.3		
E_1	(*TO*)	362.1	346.3	329.1	312.0	295.7	278.7	270.9	265.0	250.2	235.7	221.8	277.6	273.3
	(*LO*)	427.5	414.7	401.1	387.4	374.6	361.5	355.7	351.1	339.8	329.0	318.6	337.3	351.1
	Δ	65.4	68.4	71.9	75.4	78.9	82.8	84.7	86.1	89.7	93.3	96.8		
E_2	(*TO*)	376.3	359.1	340.1	321.6	303.8	285.1	276.6	270.4	254.2	238.3	223.4	283.4	286.0
B	(*TO*)	422.2	404.4	386.5	370.3	354.6	338.6	331.5	326.3	313.7	302.2	291.7	283.4	286.0

Notes: Δ is the difference between the longitudinal and transversal optical frequency.
† Kang et al. (2017)
‡ Brafman and Mitra (1968)

Table 5. DFT/B3LYP wz-ZnS molar volume, coefficient of thermal expansion (α_V), isothermal bulk modulus (K_T) and its pressure derivative (K_T'), adiabatic bulk modulus (K_S), entropy (S) and isobaric heat capacity (C_P) in the pressure range 0 – 20 GPa and at 300 K. In brackets, the standard deviations calculated by the volume-integrated 3rd-order Birch-Murnaghan equation of state are reported.

P (GPa)	V (Å^3 mol^{-1})	α_V (10^{-6} K^{-1})	K_T (GPa)	K_T'	K_S (GPa)	S (J mol^{-1} K^{-1})	C_P (J mol^{-1} K^{-1})
0	43.22(2)	21.635	68.6(6)	4.01(13)	68.9	58.49	45.46
1	42.61(2)	18.777	72.6(5)	4.00(12)	72.8	57.98	45.25
2	42.04(2)	16.592	76.5(4)	3.95(12)	76.8	57.51	45.06
3	41.51(2)	16.299	80.5(3)	3.91(12)	80.8	57.10	44.92
4	41.01(2)	14.341	84.4(3)	3.86(12)	84.6	56.73	44.74
5	40.54(3)	13.230	88.(3)	3.82(12)	88.5	56.40	44.59
6	40.09(2)	11.440	92.1(3)	3.78(12)	92.2	56.11	44.42
7	39.67(3)	10.333	95.8(4)	3.73(12)	96.0	55.84	44.27
8	39.26(2)	9.226	99.6(5)	3.69(12)	99.7	55.61	44.13
9	38.88(2)	8.525	103.2(6)	3.65(12)	103.4	55.40	43.99
10	38.51(2)	7.702	106.9(7)	3.61(12)	107.0	55.21	43.85
11	38.16(2)	6.771	110.5(8)	3.57(12)	110.5	55.05	43.72
12	37.82(2)	6.142	114.0(9)	3.52(12)	114.1	54.90	43.59
13	37.49(2)	5.724	118(1)	3.49(12)	117.6	54.78	43.46
14	37.18(2)	4.250	121(1)	3.44(12)	120.9	54.66	43.33
15	36.88(3)	3.983	124(1)	3.40(12)	124.3	54.57	43.21
16	36.59(3)	4.187	128(1)	3.36(13)	127.7	54.48	43.09
17	36.30(4)	3.471	131(2)	3.32(12)	131.0	54.41	42.97
18	36.03(4)	1.520	134(2)	3.28(13)	134.2	54.36	42.85
19	35.77(5)	-0.245	137(2)	3.24(13)	137.3	54.31	42.73
20	35.51(6)	1.352	140(2)	3.20(13)	140.4	54.27	42.62

Fig 1

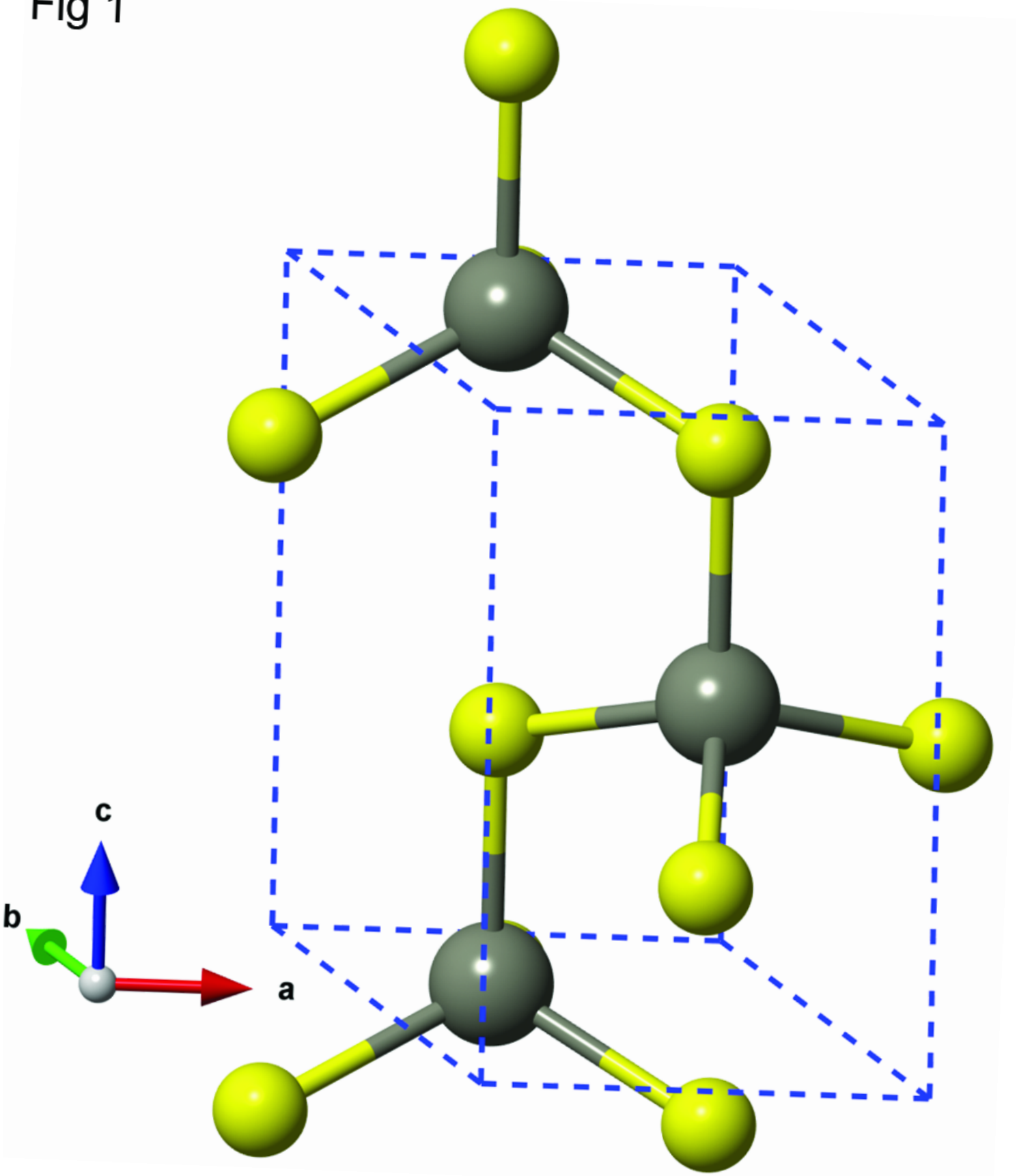

Fig 2a

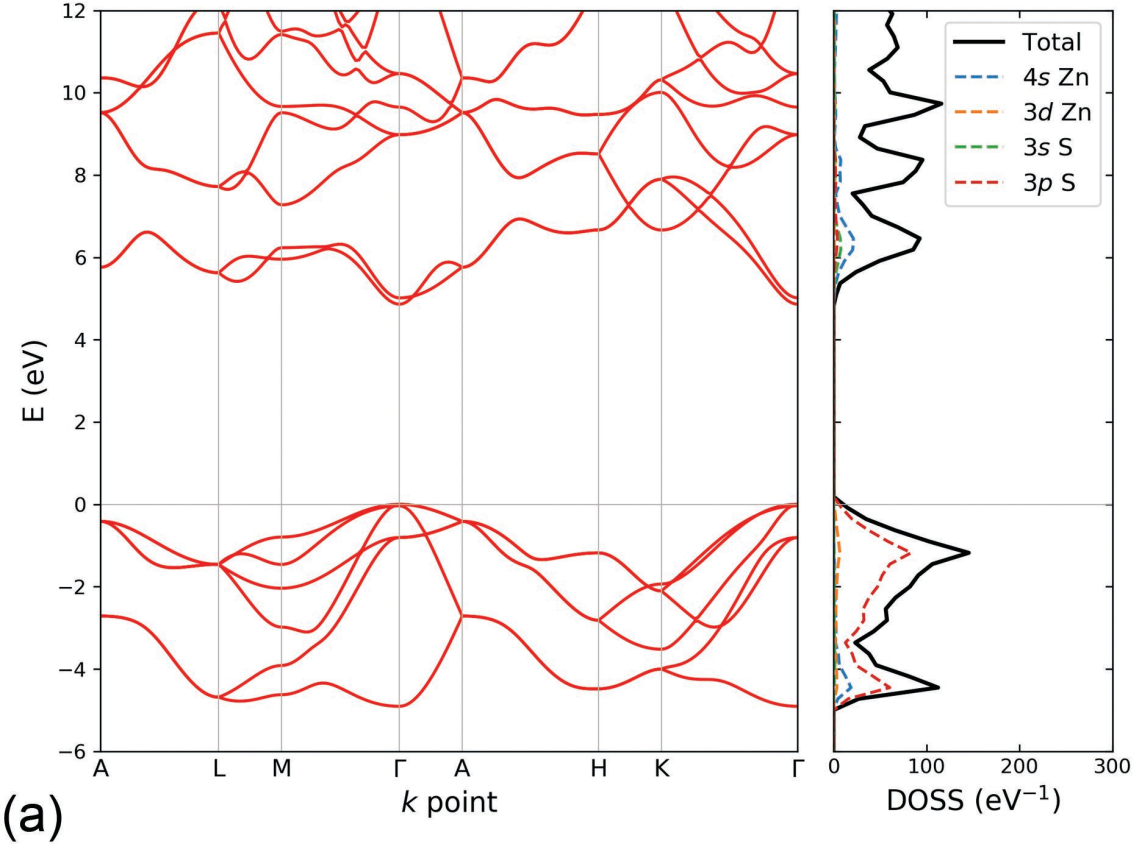
12
10
8
6
4
2
0
−2
−4
−6
E (eV)
A
L
M
Γ
A
H
K
Γ
k point
Total
4s Zn
3d Zn
3s S
3p S
0
100
200
300
DOSS (eV^{-1})

(a)

Fig 2b

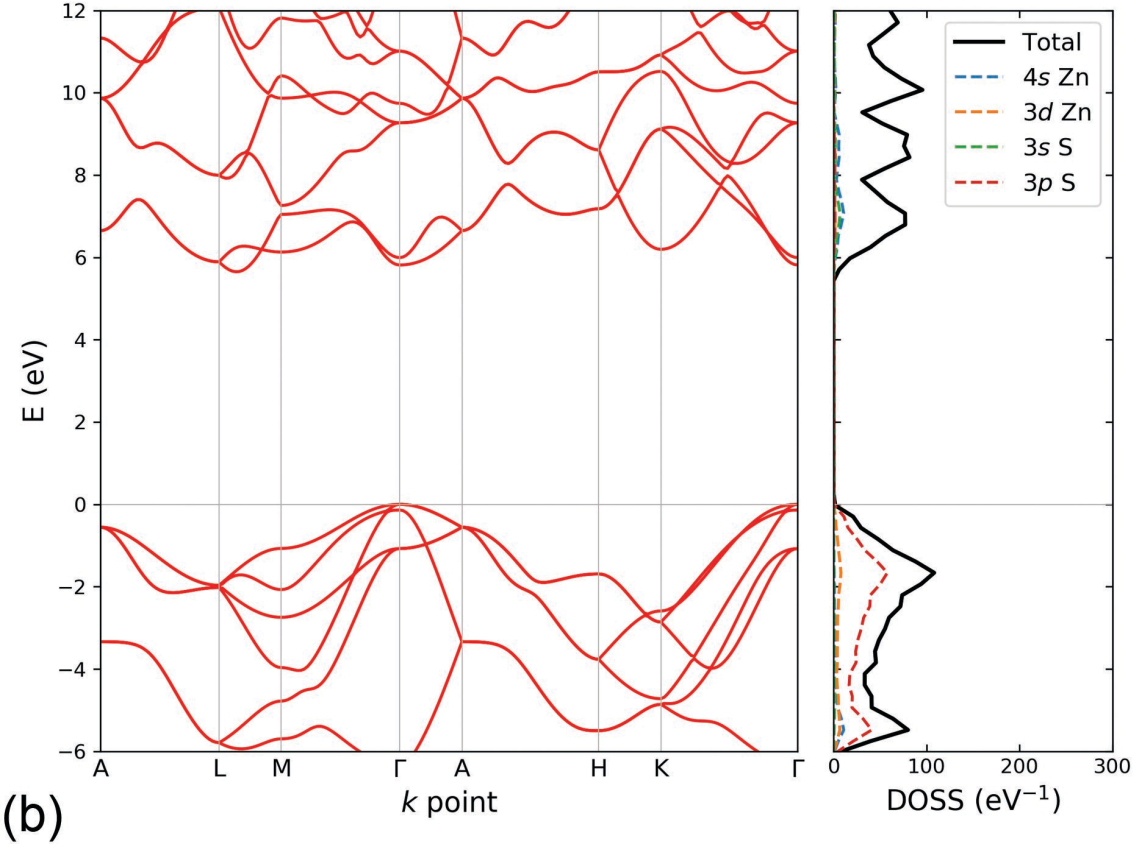
12
10
8
6
4
2
0
−2
−4
−6
E (eV)
A
L
M
Γ
A
H
K
Γ
k point
Total
4s Zn
3d Zn
3s S
3p S
0
100
200
300
DOSS (eV−1)

(b)

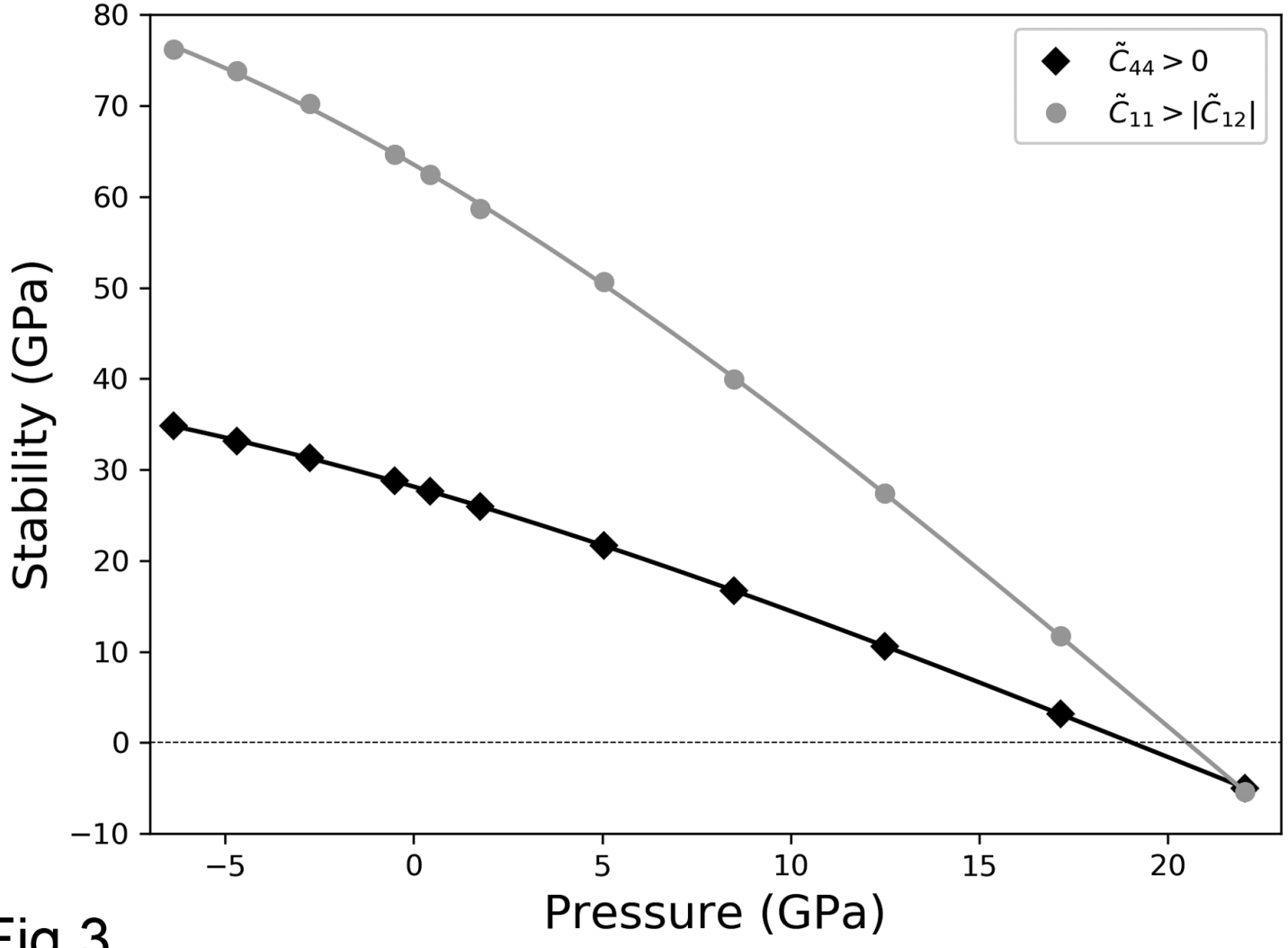
80
70
60
50
40
30
20
10
0
−10
−5
0
5
10
15
20
Stability (GPa)
Pressure (GPa)
$\tilde{C}_{44} > 0$
$\tilde{C}_{11} > |\tilde{C}_{12}|$

Fig 3

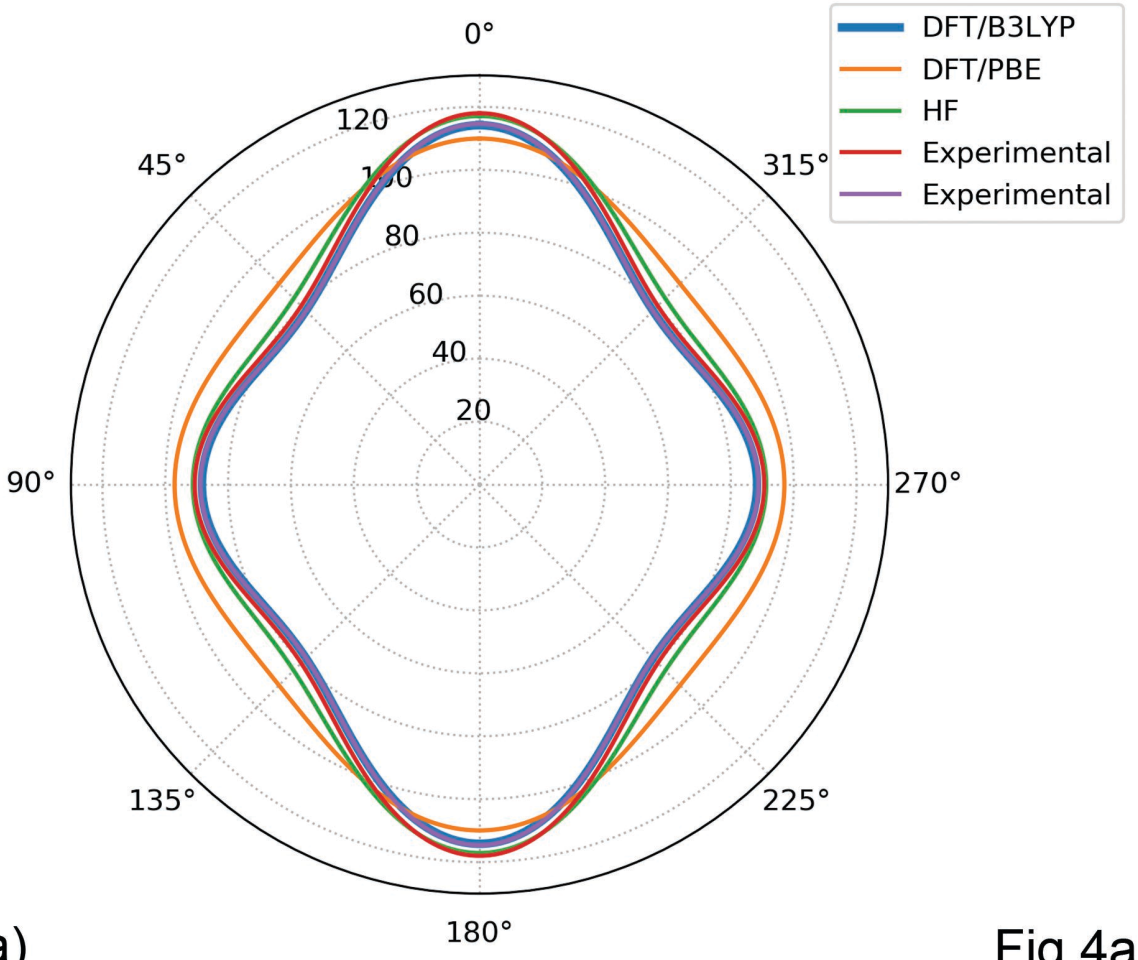
DFT/B3LYP
DFT/PBE
HF
Experimental
Experimental
0°
45°
315°
90°
270°
135°
225°
180°
120
80
60
40
20

(a)

Fig 4a

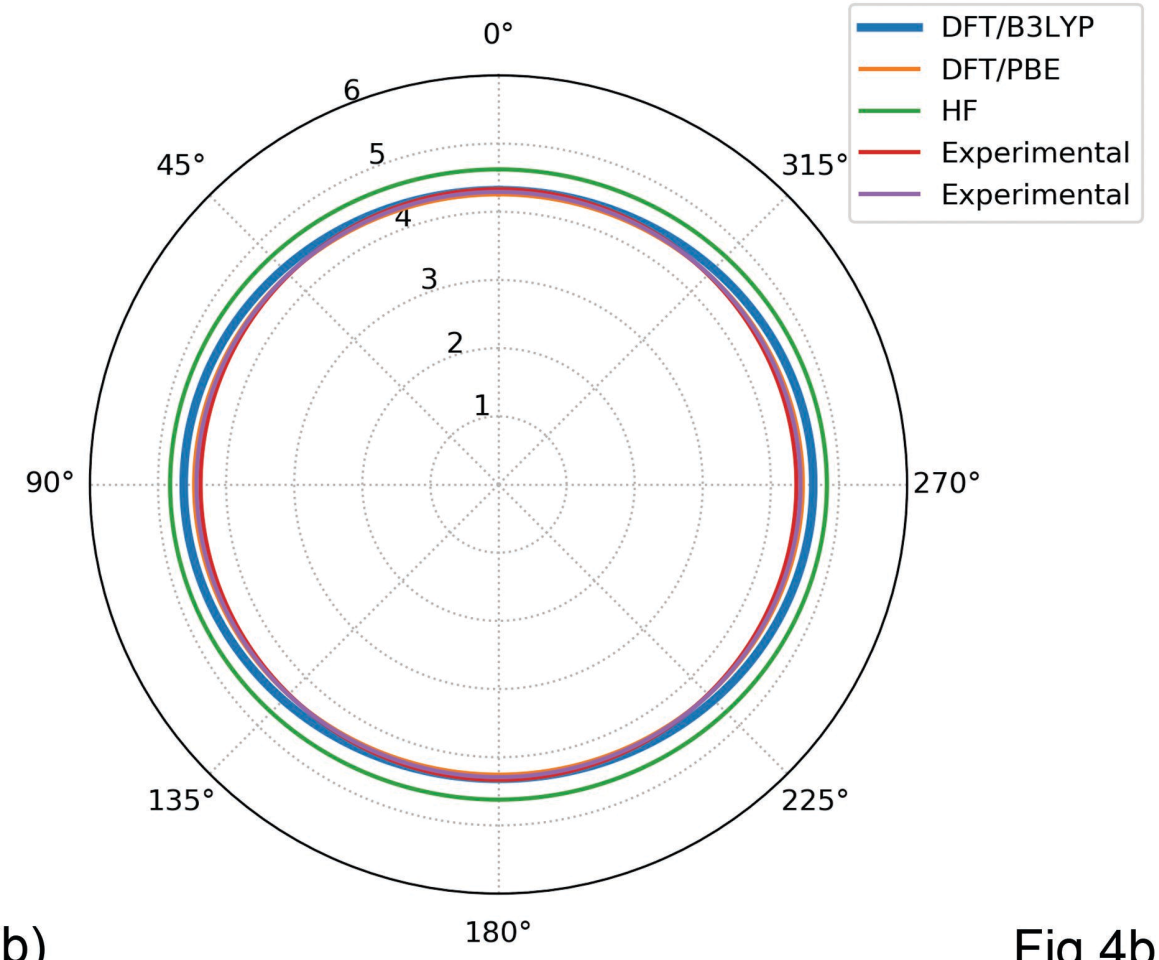
DFT/B3LYP
DFT/PBE
HF
Experimental
Experimental
0°
45°
90°
135°
180°
225°
270°
315°
1
2
3
4
5
6

(b)

Fig 4b

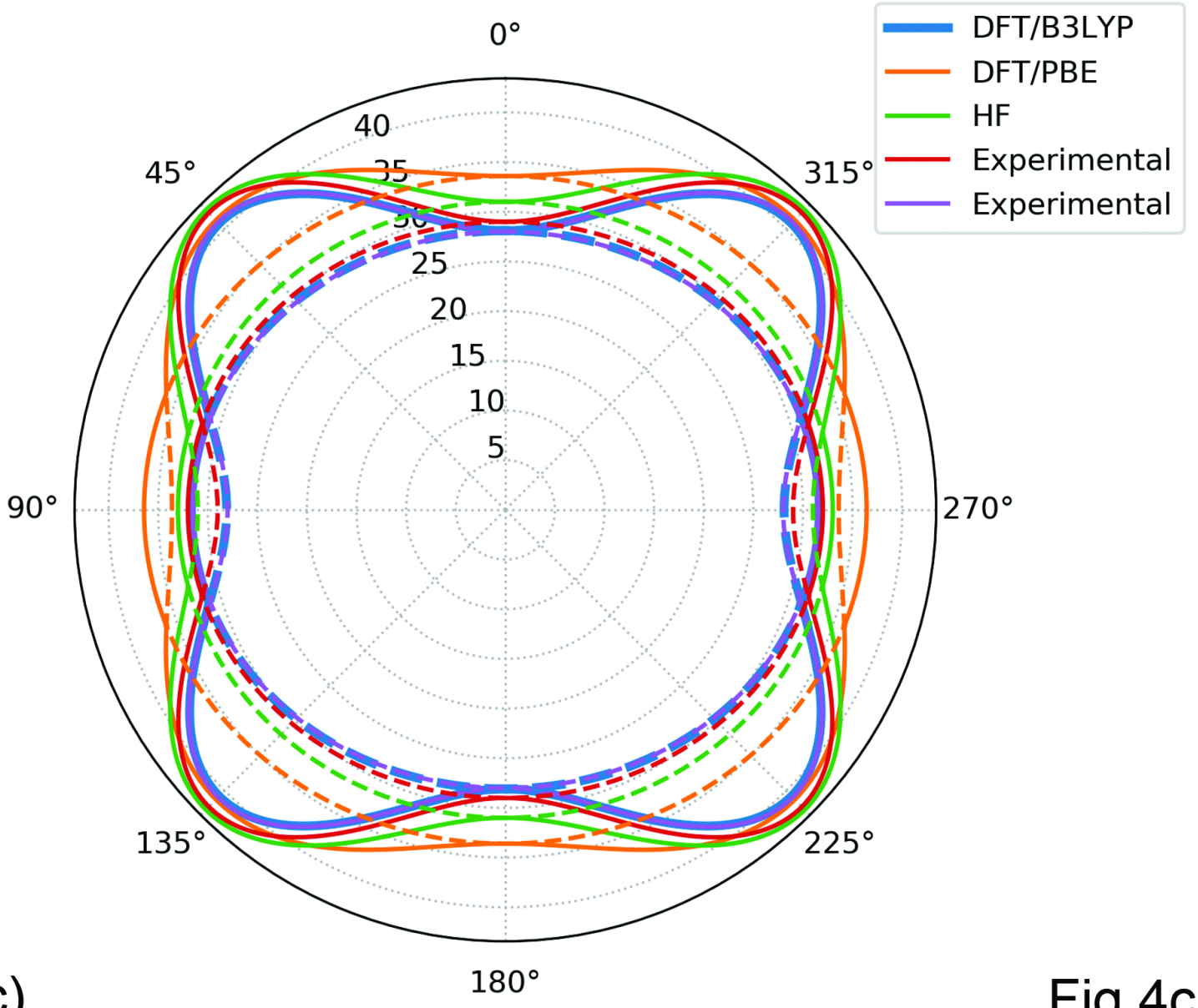
DFT/B3LYP
DFT/PBE
HF
Experimental
Experimental
0°
45°
315°
90°
270°
135°
225°
180°
40
35
25
20
15
10
5

(c)

Fig 4c

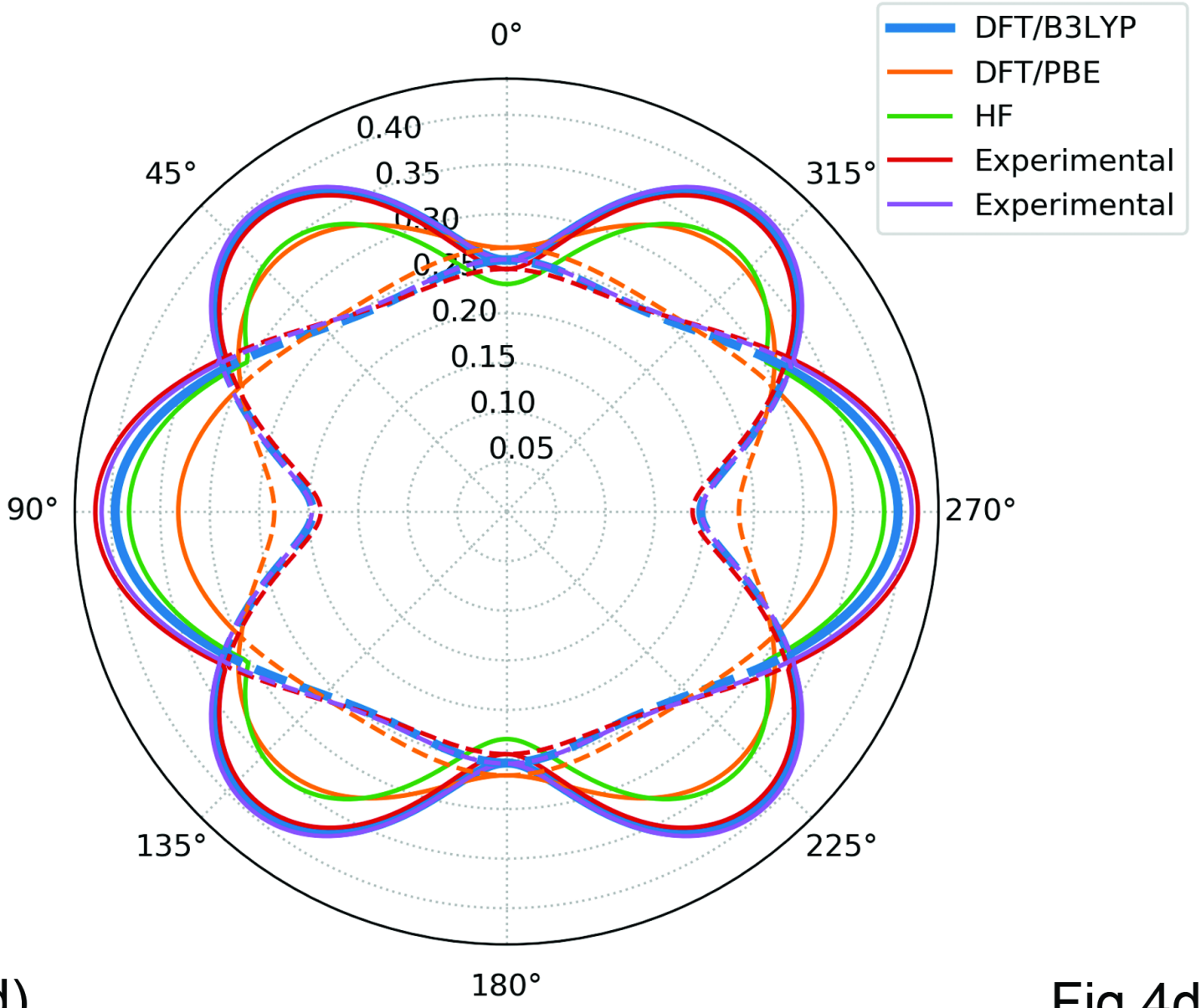
DFT/B3LYP
DFT/PBE
HF
Experimental
Experimental
0°
45°
315°
90°
270°
135°
225°
180°
0.40
0.35
0.30
0.25
0.20
0.15
0.10
0.05

(d)

Fig 4d

Fig 5a

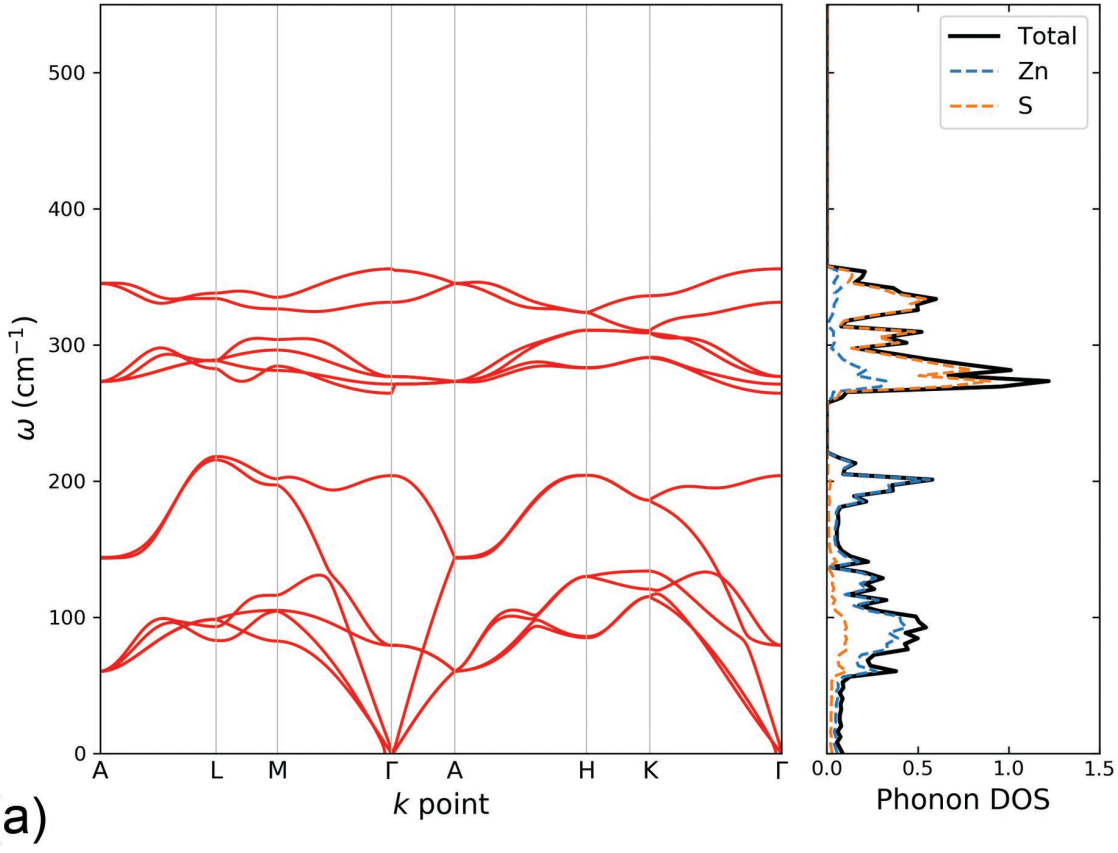
500
400
300
200
100
0
ω (cm⁻¹)
A
L
M
Γ
A
H
K
Γ
k point
Total
Zn
S
0.0
0.5
1.0
1.5
Phonon DOS

(a)

Fig 5b

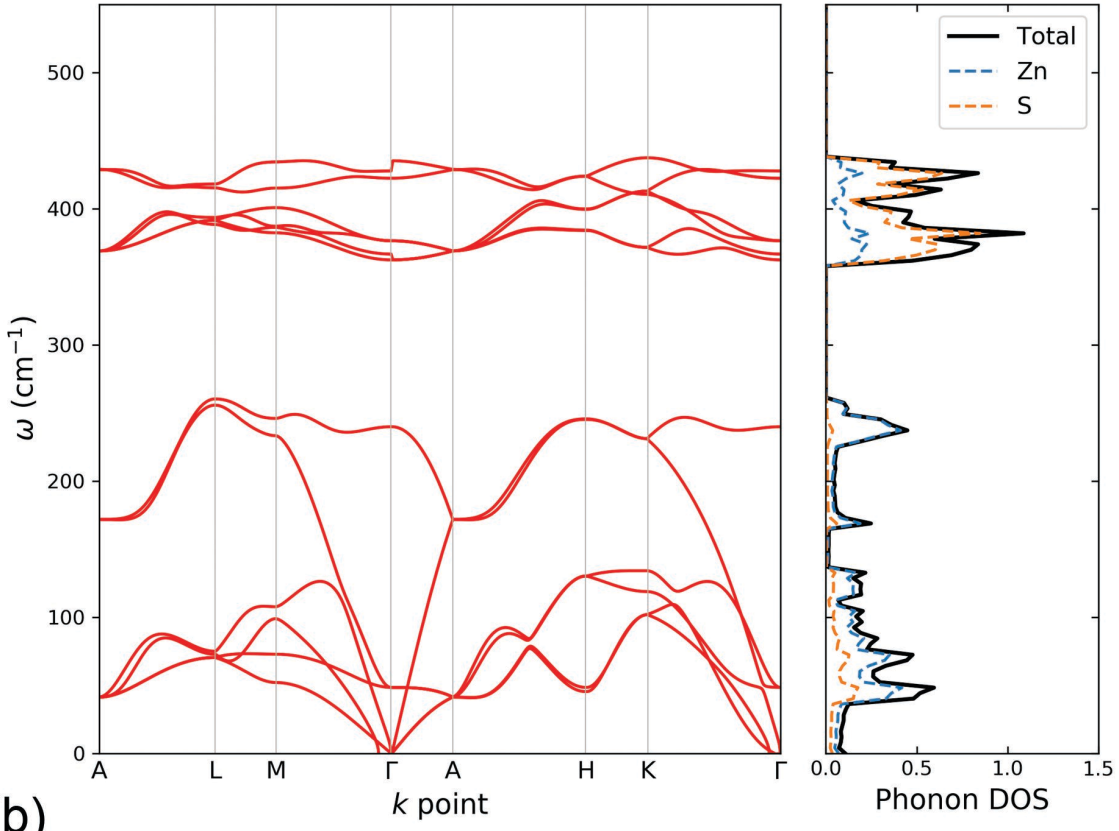
500
400
300
200
100
0
ω (cm⁻¹)
A
L
M
Γ
A
H
K
Γ
k point
Total
Zn
S
0.0
0.5
1.0
1.5
Phonon DOS

(b)

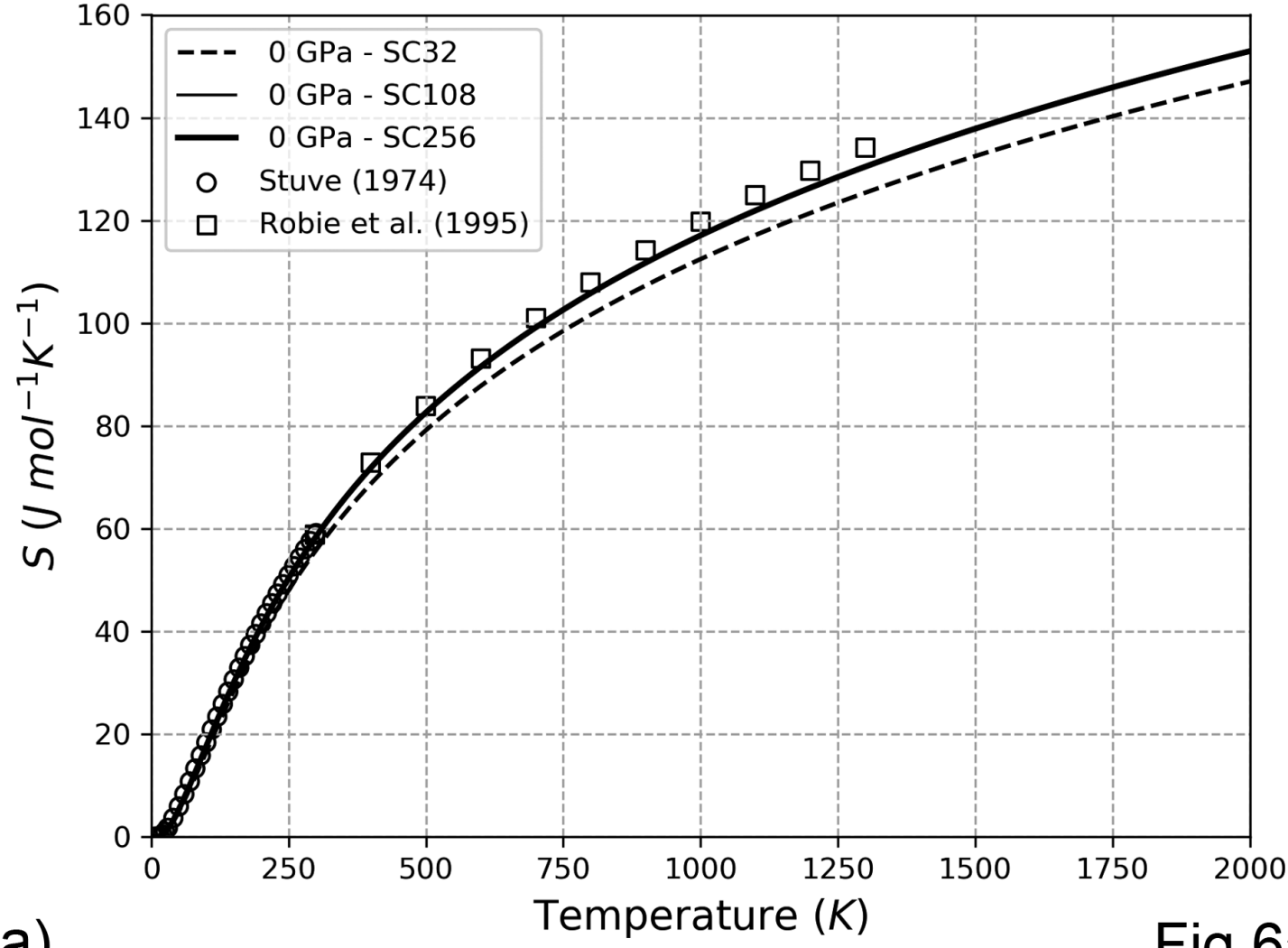
0 GPa - SC32
0 GPa - SC108
0 GPa - SC256
Stuve (1974)
Robie et al. (1995)
S (J mol⁻¹K⁻¹)
Temperature (K)
0
20
40
60
80
100
120
140
160
0
250
500
750
1000
1250
1500
1750
2000

(a)

Fig 6a

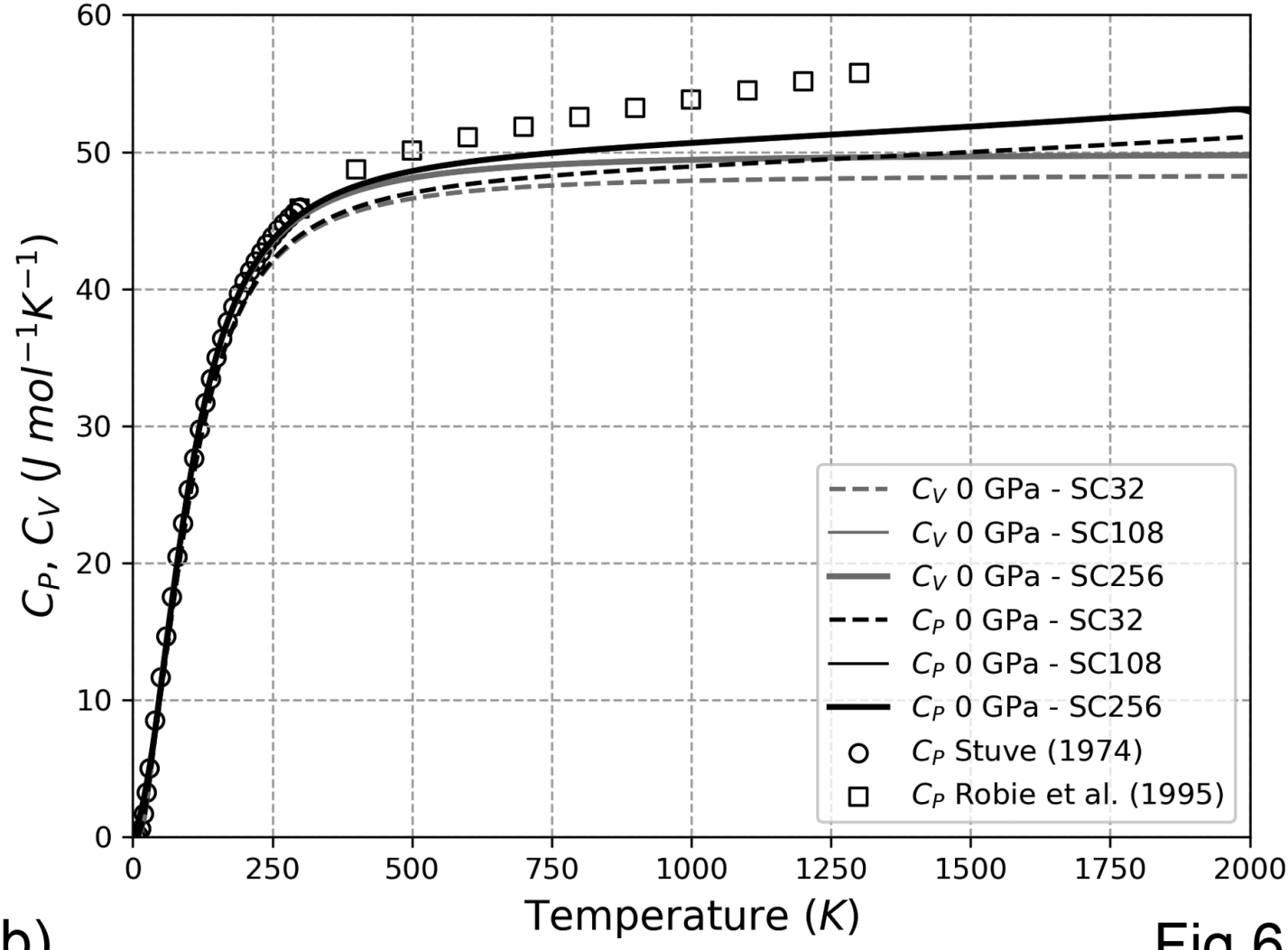
60
50
40
30
20
10
0
0
250
500
750
1000
1250
1500
1750
2000
C_P, C_V ($J\ mol^{-1}K^{-1}$)
Temperature (K)
C_V 0 GPa - SC32
C_V 0 GPa - SC108
C_V 0 GPa - SC256
C_P 0 GPa - SC32
C_P 0 GPa - SC108
C_P 0 GPa - SC256
C_P Stuve (1974)
C_P Robie et al. (1995)

(b)

Fig 6b

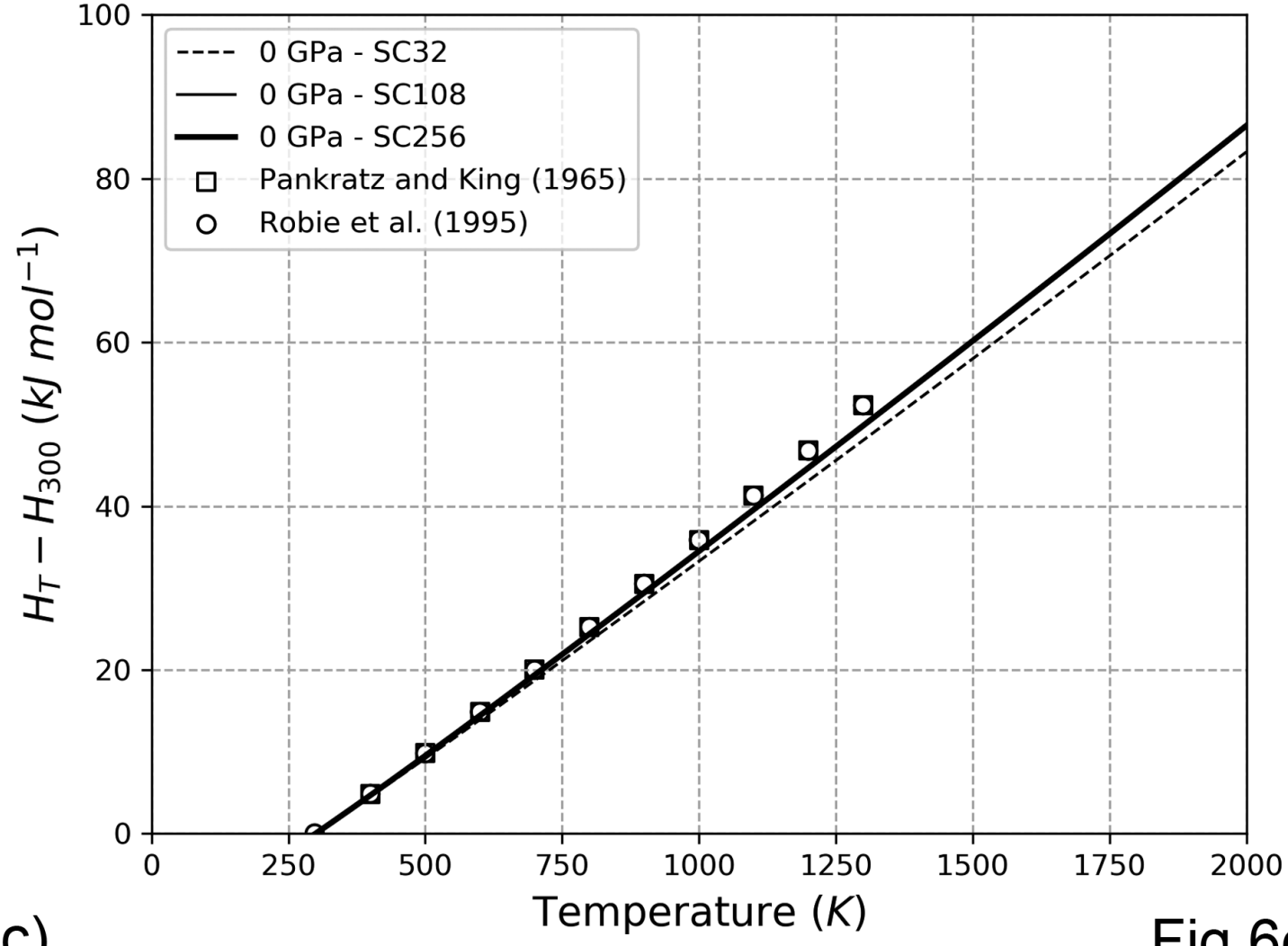
0 GPa - SC32
0 GPa - SC108
0 GPa - SC256
Pankratz and King (1965)
Robie et al. (1995)
$H_T - H_{300}$ ($kJ\ mol^{-1}$)
Temperature (K)
0
20
40
60
80
100
0
250
500
750
1000
1250
1500
1750
2000

(c)

Fig 6c

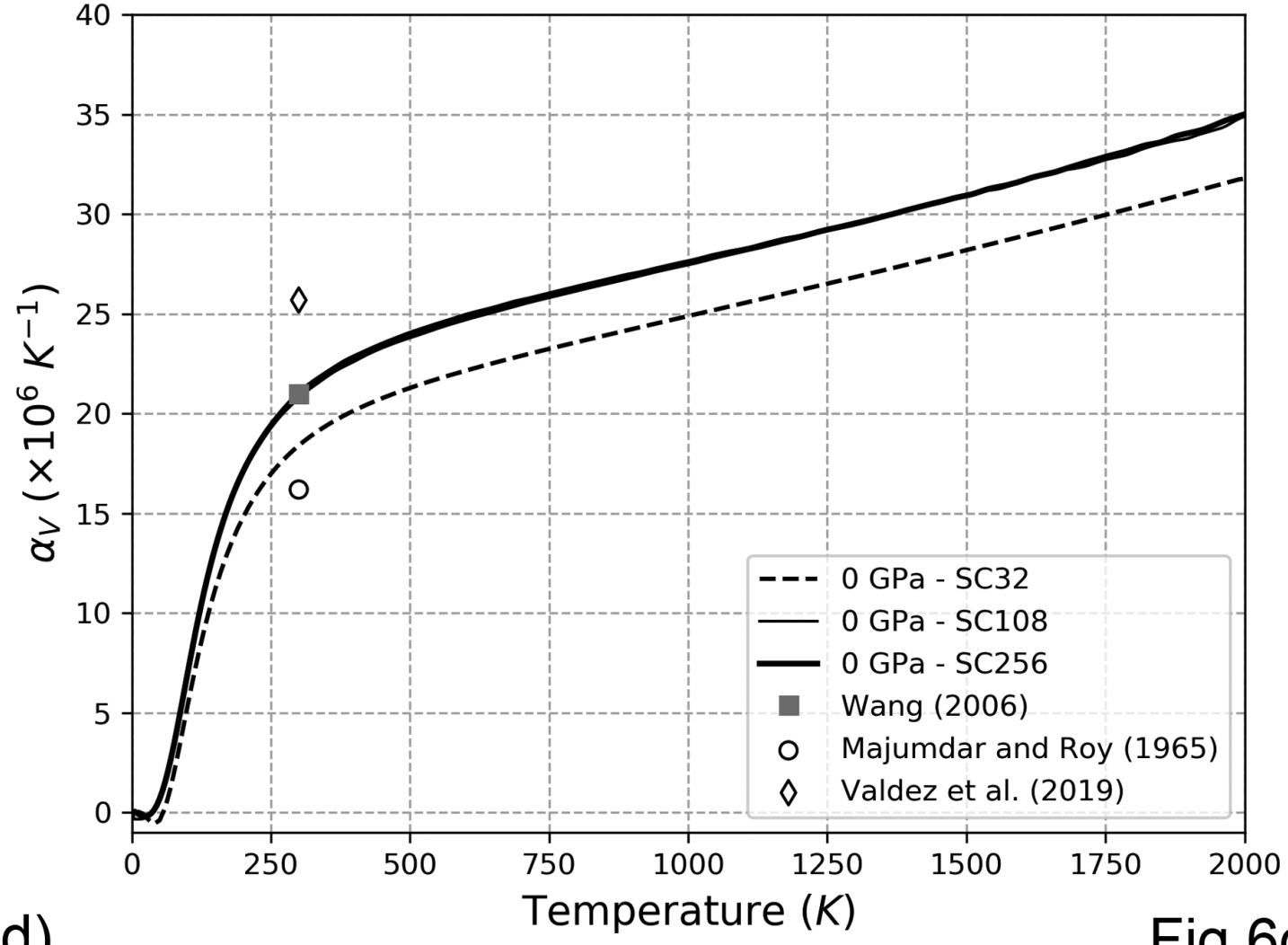
40
35
30
25
20
15
10
5
0
α_V ($\times 10^6$ K^{-1})
0
250
500
750
1000
1250
1500
1750
2000
Temperature (K)
0 GPa - SC32
0 GPa - SC108
0 GPa - SC256
Wang (2006)
Majumdar and Roy (1965)
Valdez et al. (2019)

(d)

Fig 6d

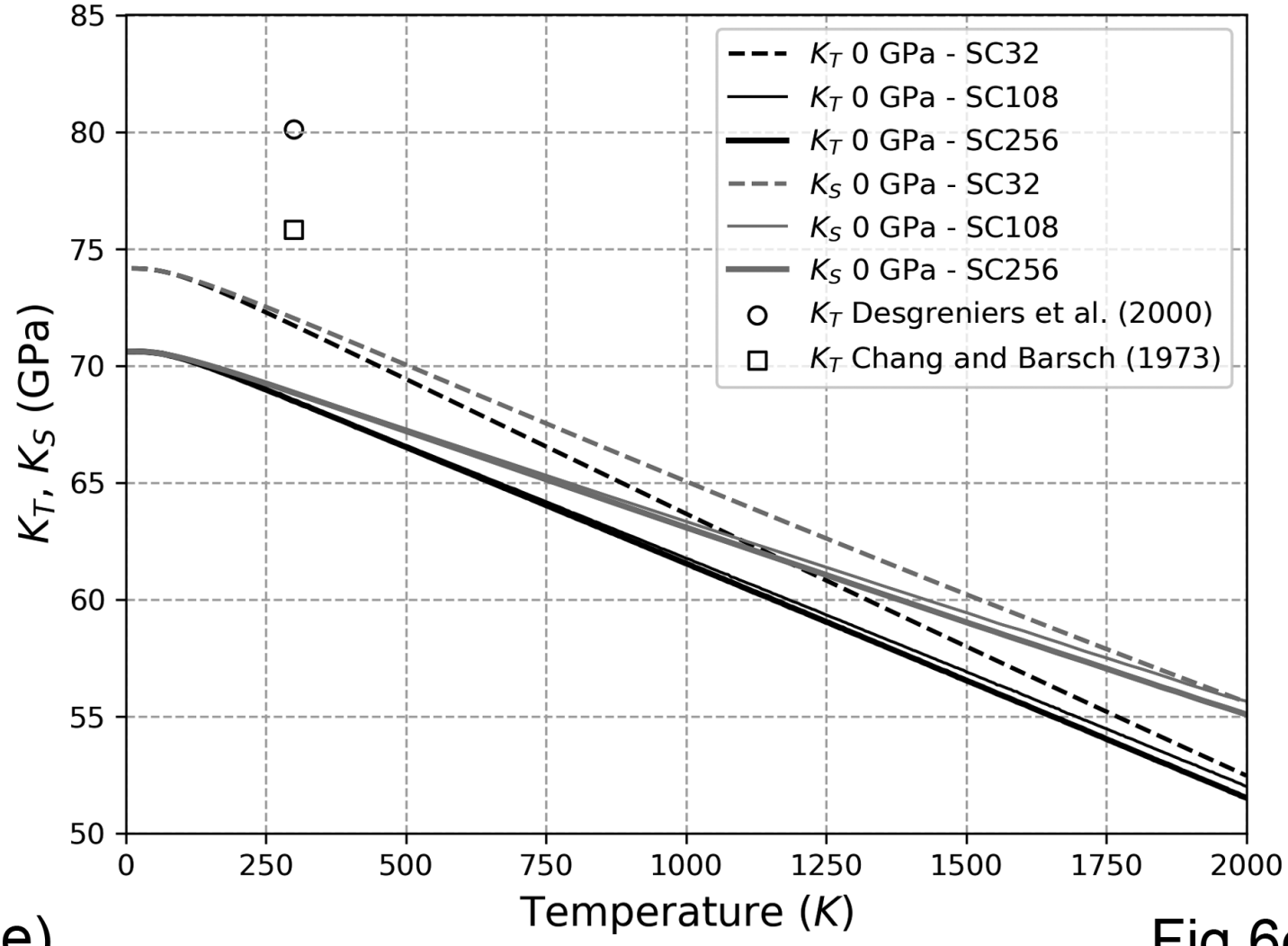
85
80
75
70
65
60
55
50
0
250
500
750
1000
1250
1500
1750
2000
K_T, K_S (GPa)
Temperature (K)
K_T 0 GPa - SC32
K_T 0 GPa - SC108
K_T 0 GPa - SC256
K_S 0 GPa - SC32
K_S 0 GPa - SC108
K_S 0 GPa - SC256
K_T Desgreniers et al. (2000)
K_T Chang and Barsch (1973)

(e)

Fig 6e

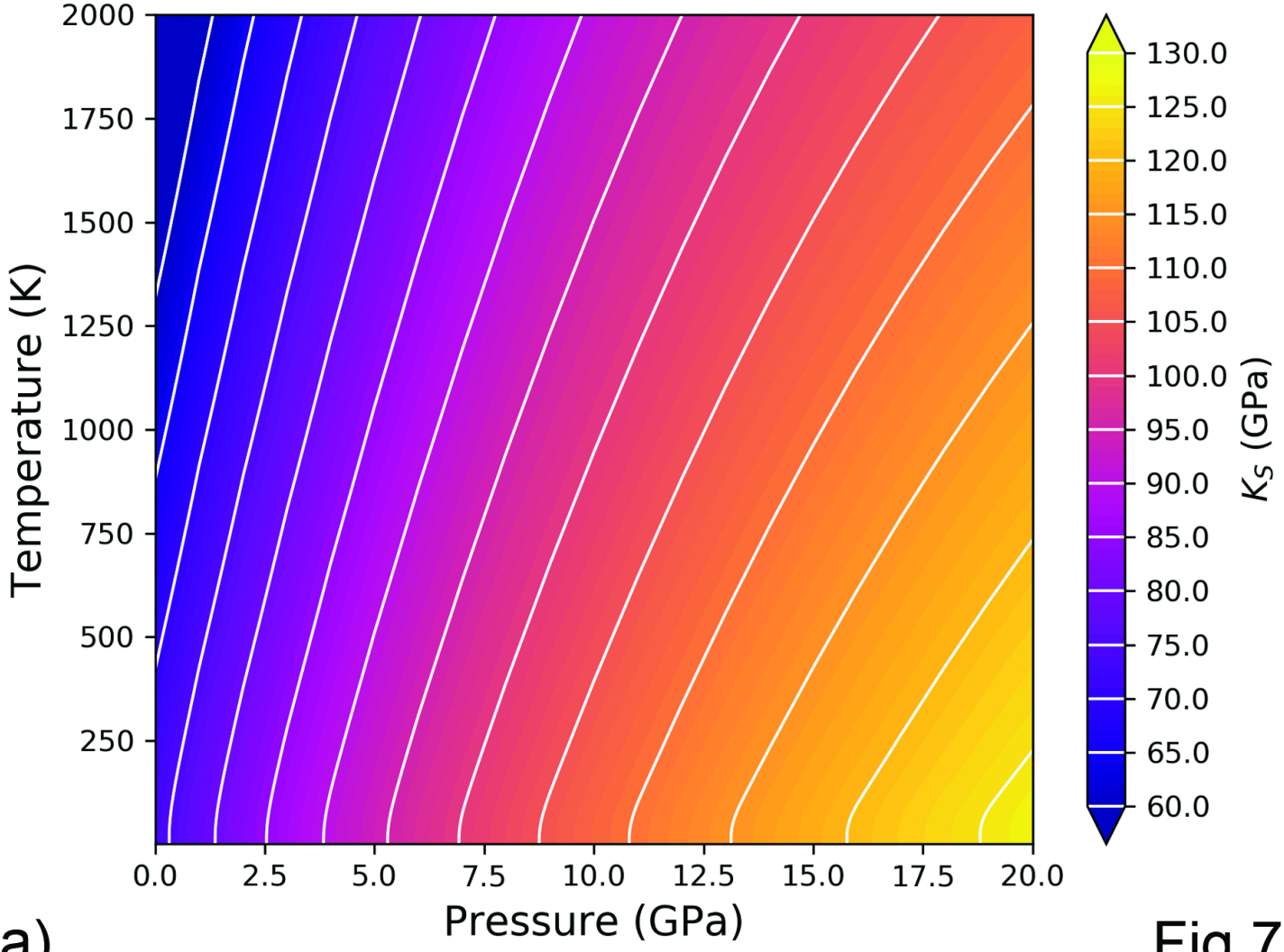
2000
1750
1500
1250
1000
750
500
250
Temperature (K)
0.0
2.5
5.0
7.5
10.0
12.5
15.0
17.5
20.0
Pressure (GPa)
130.0
125.0
120.0
115.0
110.0
105.0
100.0
95.0
90.0
85.0
80.0
75.0
70.0
65.0
60.0
K_S (GPa)

(a)

Fig 7a

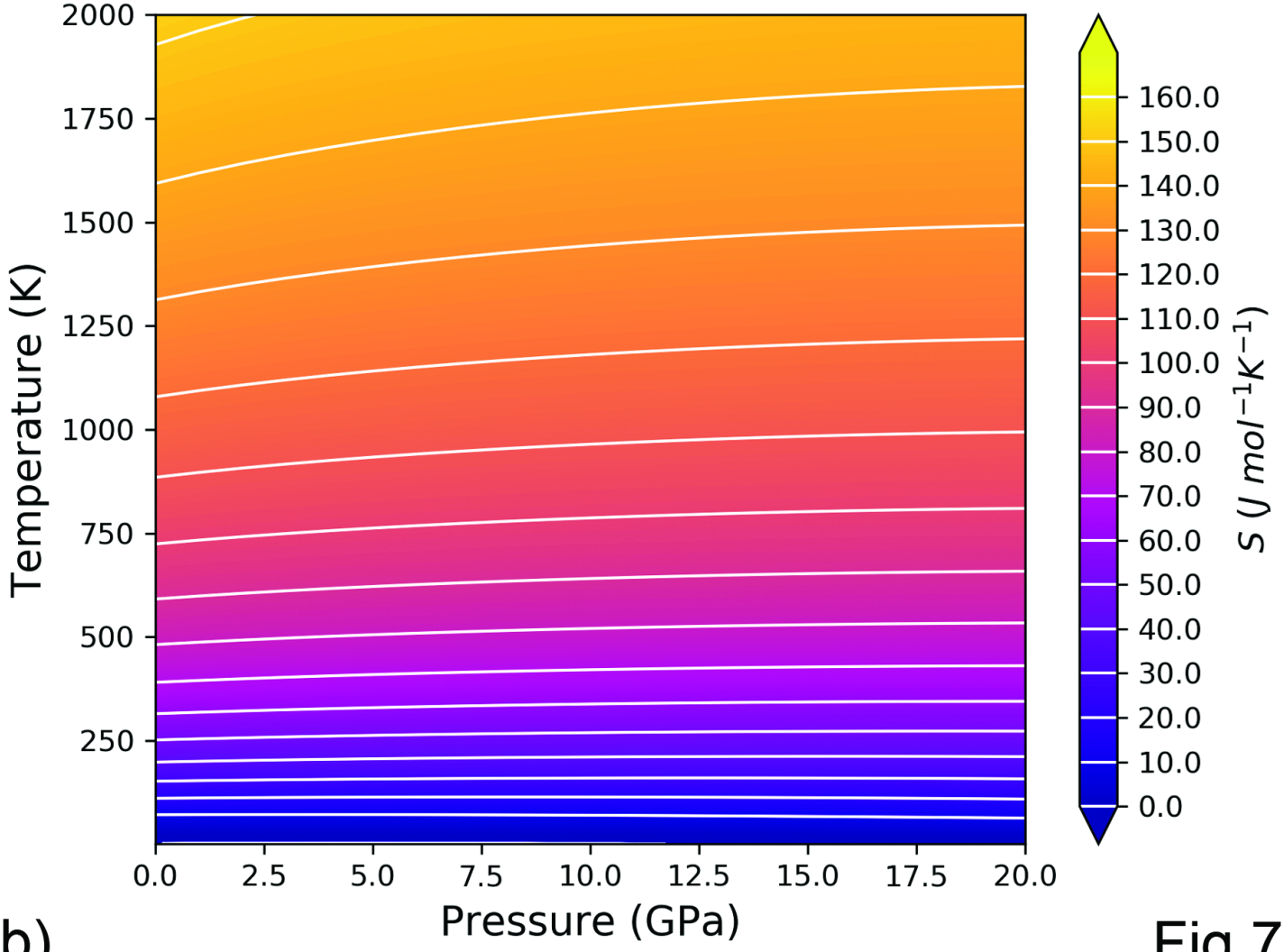
2000
1750
1500
1250
1000
750
500
250
Temperature (K)
0.0
2.5
5.0
7.5
10.0
12.5
15.0
17.5
20.0
Pressure (GPa)
160.0
150.0
140.0
130.0
120.0
110.0
100.0
90.0
80.0
70.0
60.0
50.0
40.0
30.0
20.0
10.0
0.0
S (J mol⁻¹K⁻¹)

(b)

Fig 7b

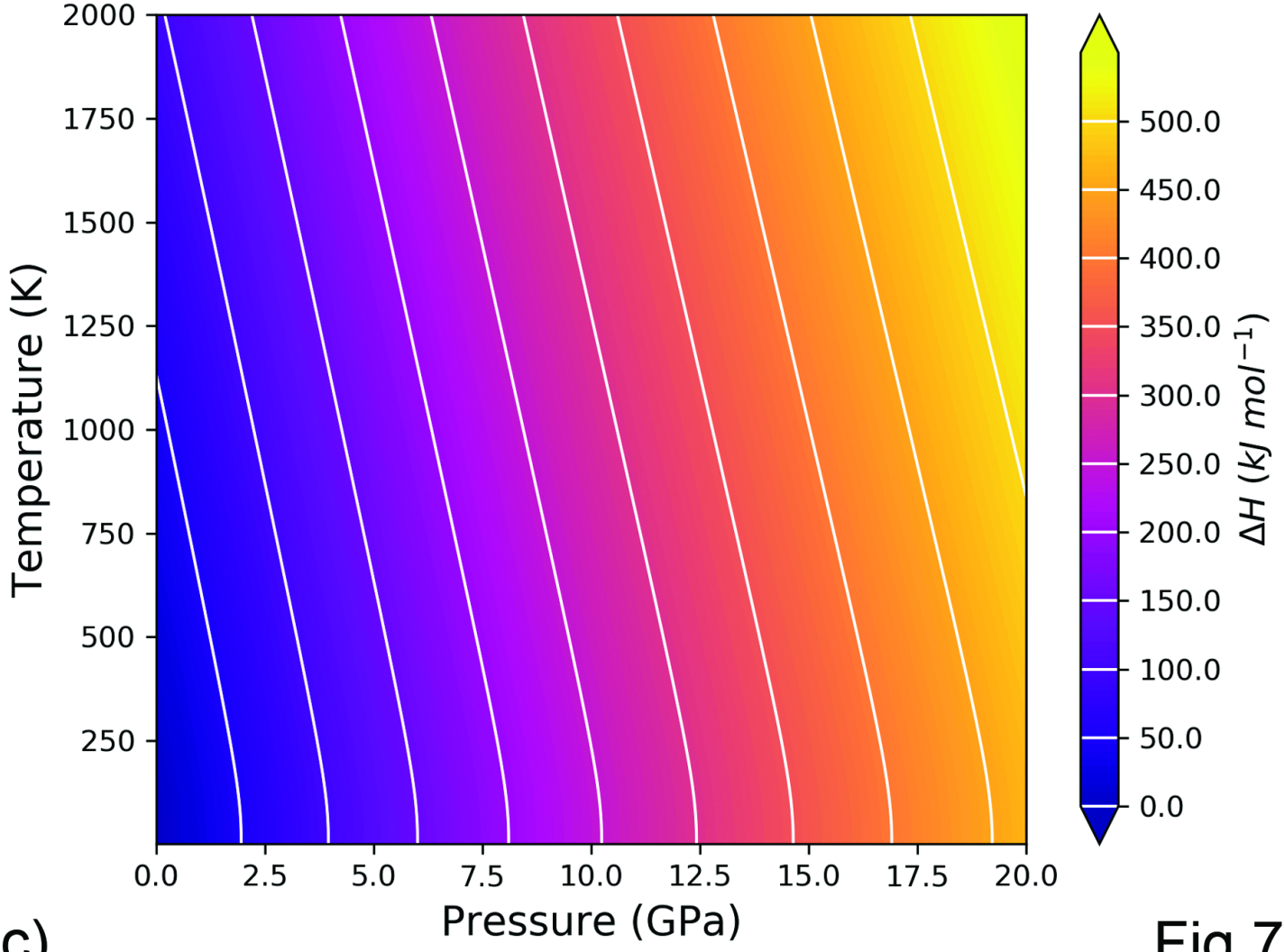
2000
1750
1500
1250
1000
750
500
250
Temperature (K)
0.0
2.5
5.0
7.5
10.0
12.5
15.0
17.5
20.0
Pressure (GPa)
500.0
450.0
400.0
350.0
300.0
250.0
200.0
150.0
100.0
50.0
0.0
ΔH (kJ mol⁻¹)

(c)

Fig 7c

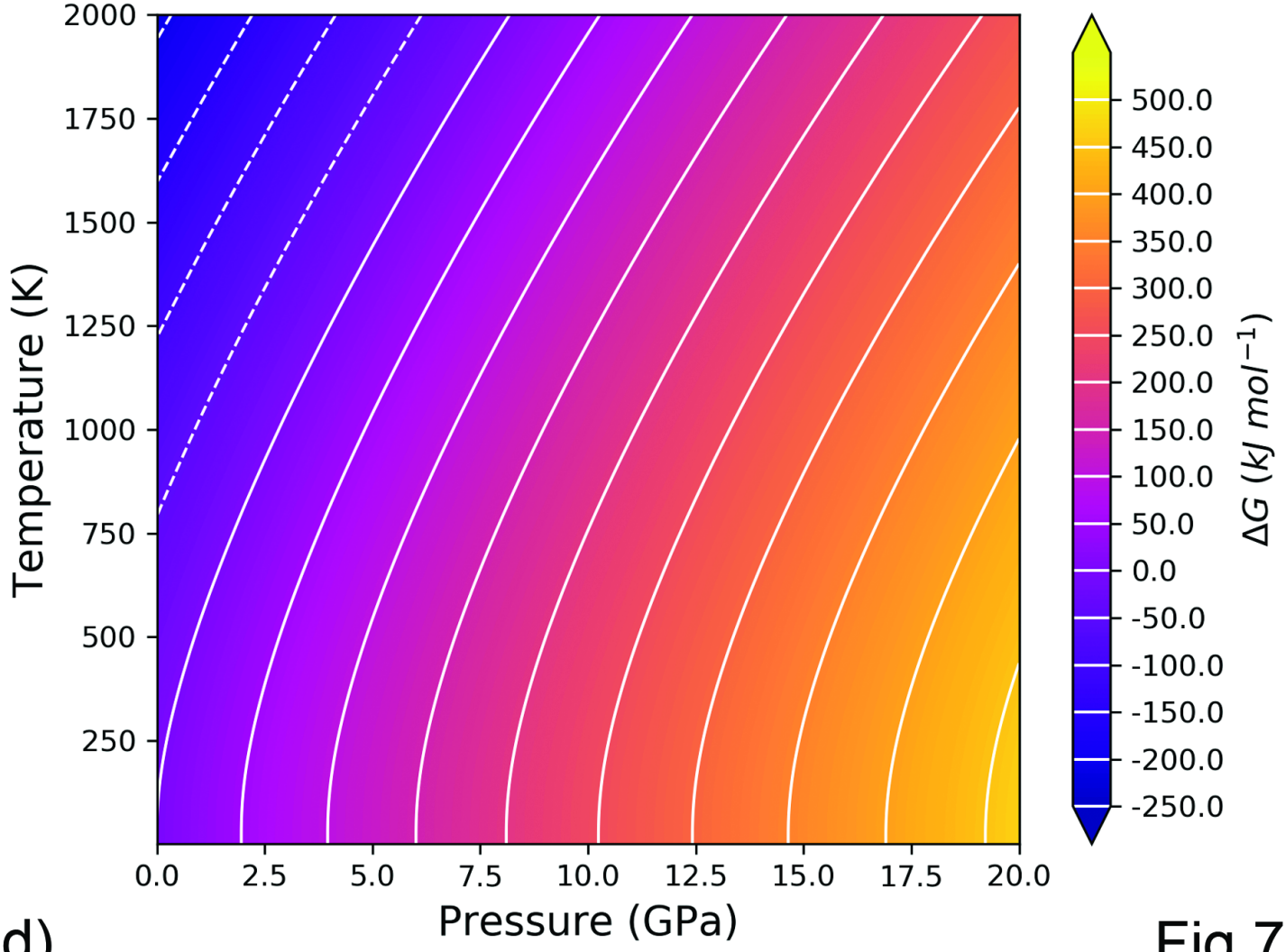
2000
1750
1500
1250
1000
750
500
250
Temperature (K)
0.0
2.5
5.0
7.5
10.0
12.5
15.0
17.5
20.0
Pressure (GPa)
500.0
450.0
400.0
350.0
300.0
250.0
200.0
150.0
100.0
50.0
0.0
-50.0
-100.0
-150.0
-200.0
-250.0
ΔG (kJ mol⁻¹)

(d)

Fig 7d

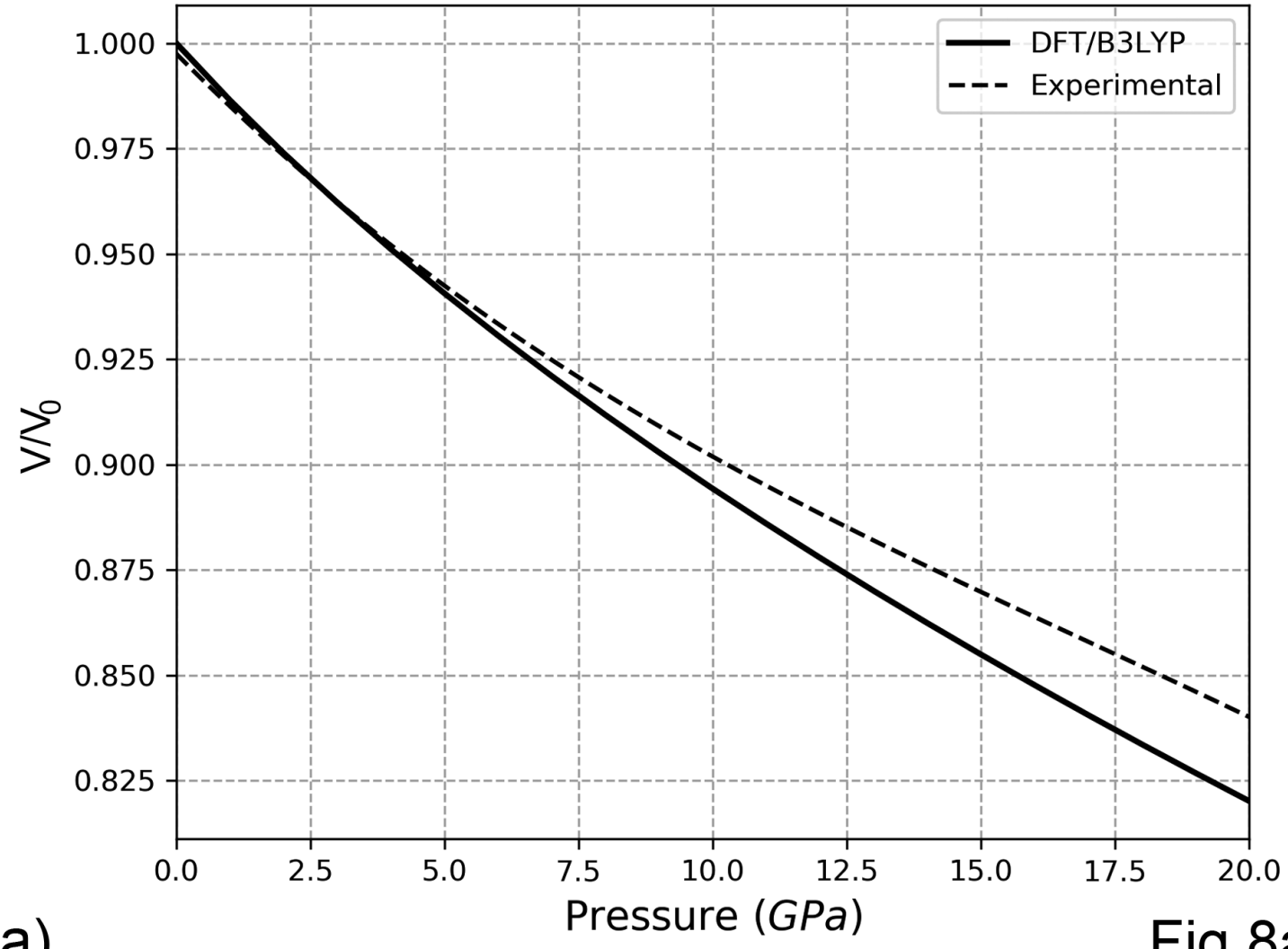
DFT/B3LYP
Experimental
1.000
0.975
0.950
0.925
0.900
0.875
0.850
0.825
V/V0
0.0
2.5
5.0
7.5
10.0
12.5
15.0
17.5
20.0
Pressure (GPa)

(a)

Fig 8a

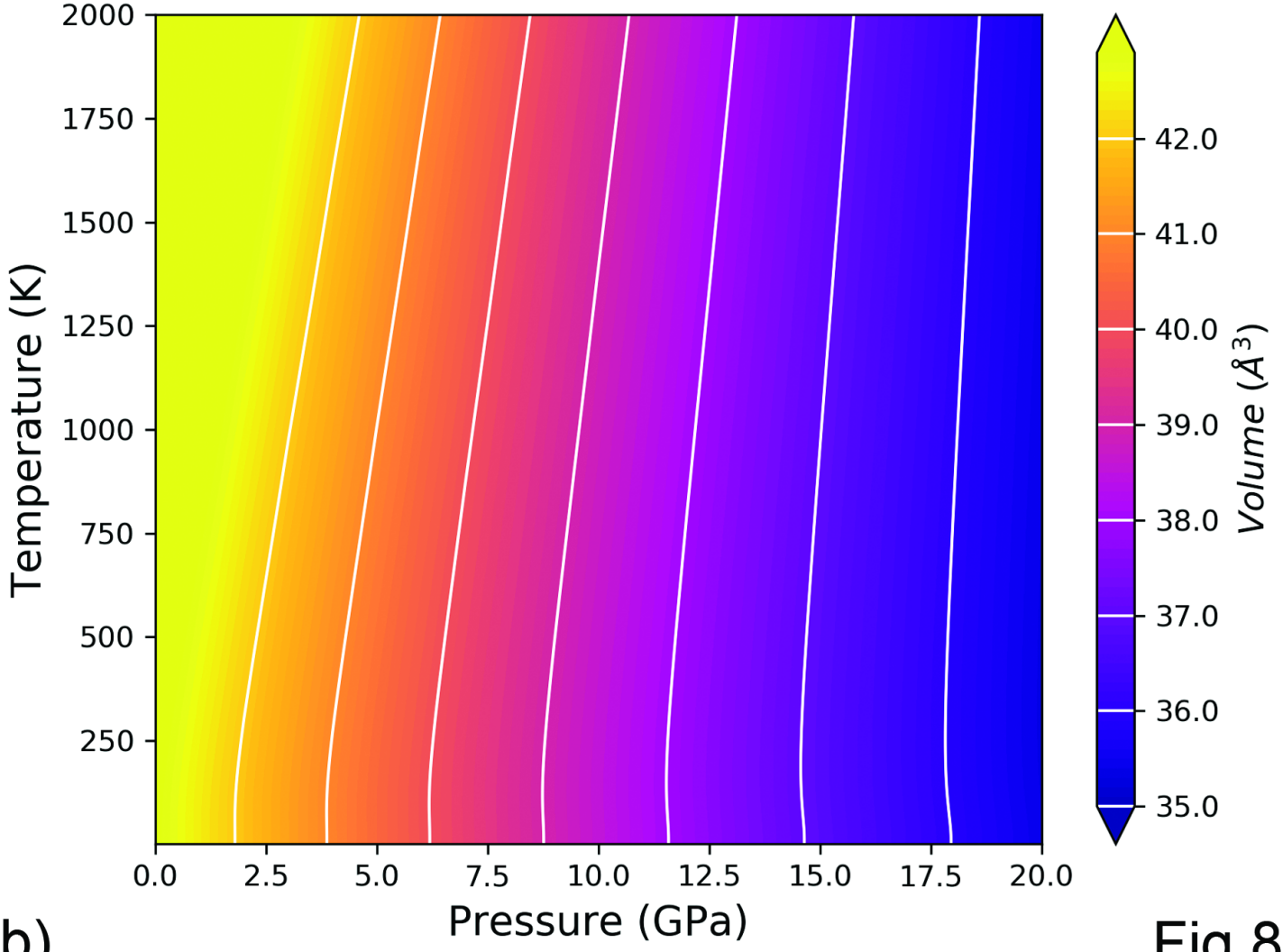
2000
1750
1500
1250
1000
750
500
250
Temperature (K)
0.0
2.5
5.0
7.5
10.0
12.5
15.0
17.5
20.0
Pressure (GPa)
42.0
41.0
40.0
39.0
38.0
37.0
36.0
35.0
Volume (Å³)

(b)

Fig 8b